



# ALMA and IRIS Observations of the Solar Chromosphere. II. Structure and Dynamics of Chromospheric Plages

Georgios Chintzoglou<sup>1,2</sup> , Bart De Pontieu<sup>1,3,4</sup> , Juan Martínez-Sykora<sup>1,3,5</sup> , Viggo Hansteen<sup>1,3,4,5</sup> ,  
Jaime de la Cruz Rodríguez<sup>6</sup> , Mikolaj Szydlarski<sup>3,4</sup> , Shahin Jafarzadeh<sup>3,4</sup> , Sven Wedemeyer<sup>3,4</sup> , Timothy S. Bastian<sup>7</sup> , and  
Alberto Sainz Dalda<sup>1,5,8</sup>

<sup>1</sup> Lockheed Martin Solar & Astrophysics Laboratory, Palo Alto, CA 94304, USA; [gchintzo@lmsal.com](mailto:gchintzo@lmsal.com)

<sup>2</sup> University Corporation for Atmospheric Research, Boulder, CO 80307-3000, USA

<sup>3</sup> Rosseland Center for Solar Physics, University of Oslo, P.O. Box 1029 Blindern, NO-0315, Oslo, Norway

<sup>4</sup> Institute of Theoretical Astrophysics, University of Oslo, P.O. Box 1029 Blindern, NO-0315, Oslo, Norway

<sup>5</sup> Bay Area Environmental Research Institute, NASA Research Park, Moffett Field, CA 94035, USA

<sup>6</sup> Institute for Solar Physics, Department of Astronomy, Stockholm University, AlbaNova University Centre, SE-106 91, Stockholm, Sweden

<sup>7</sup> National Radio Astronomy Observatory, 520 Edgemont Road, Charlottesville, VA 22903, USA

<sup>8</sup> Stanford University, HEPL, 466 Via Ortega, Stanford, CA 94305-4085, USA

Received 2020 October 19; accepted 2020 November 2; published 2021 January 12

## Abstract

We propose and employ a novel empirical method for determining chromospheric plage regions, which seems to better isolate a plage from its surrounding regions than other methods commonly used. We caution that isolating a plage from its immediate surroundings must be done with care in order to successfully mitigate statistical biases that, for instance, can impact quantitative comparisons between different chromospheric observables. Using this methodology, our analysis suggests that  $\lambda = 1.25$  mm free-free emission in plage regions observed with the Atacama Large Millimeter/submillimeter Array (ALMA)/Band6 may not form in the low chromosphere as previously thought, but rather in the upper chromospheric parts of dynamic plage features (such as spicules and other bright structures), i.e., near geometric heights of transition-region temperatures. We investigate the high degree of similarity between chromospheric plage features observed in ALMA/Band6 (at 1.25 mm wavelengths) and the Interface Region Imaging Spectrograph (IRIS)/Si IV at 1393 Å. We also show that IRIS/Mg II h and k are not as well correlated with ALMA/Band6 as was previously thought, and we discuss discrepancies with previous works. Lastly, we report indications of chromospheric heating due to propagating shocks supported by the ALMA/Band6 observations.

*Unified Astronomy Thesaurus concepts:* Solar chromosphere (1479); Solar chromospheric heating (1987); Solar electromagnetic emission (1490); Solar extreme ultraviolet emission (1493); Solar physics (1476); Solar radio emission (1522); Solar spicules (1525); Solar transition region (1532); Solar ultraviolet emission (1533)

*Supporting material:* animations

## 1. Introduction

The chromosphere is the most complex and one of the least understood layers of the solar atmosphere. It is the layer where the atmosphere transitions from a plasma-dominated to a magnetic field-dominated regime. It is a medium where ion-neutral interactions matter (such as ambipolar diffusion), and a place in the atmosphere where radiative transfer effects from departures from local thermodynamic equilibrium (LTE) are important. In addition, the chromosphere is the atmospheric shell through which energy and mass from the photosphere must pass in order to heat the overlying corona and power the solar wind.

From a modern (yet historical) observational standpoint, the chromosphere can be split into three general regions: (a) an active region (AR), sunspots and their surroundings; (b) quiet regions; and (c) regions of “plage.” The AR chromosphere plays a dominant role in energy release during intense solar flares. Often, filaments are seen to form and to erupt from neutral lines produced by flux emergence or decay (e.g., Chintzoglou et al. 2017, 2019). Sunspots seen in chromospheric wavelengths (e.g., in H $\alpha$ ) exhibit “superpenumbras,” i.e., a system of chromospheric fibril-like structures lying above the penumbra and oriented radially outward, typically extending beyond the end of the penumbra. Superpenumbras

comprise a distinct region near sunspots, commonly observed in the chromosphere of well-developed sunspots. The super-penumbra fibrils suggest, in general, a more horizontal magnetic orientation in the chromosphere, i.e., a canopy-like topology. Several studies (e.g., Yurchyshyn et al. 2001; Zhang et al. 2003) have explored the association of superpenumbras with moving magnetic features (Harvey & Harvey 1973) rushing radially outward from sunspots in the photosphere.

A major aspect of the physics of the quiet chromosphere is the ubiquitous presence of shocks, propagating from the photosphere upward (Carlsson & Stein 1997). Such shocks may play an important role in energizing the quiet chromosphere. However, the most conspicuous features of the quiet chromosphere are the so-called spicules (Secchi 1877). Spicules are jets of chromospheric material seen as rooted at the chromospheric network. About a decade ago, a new class of spicules, known as “Type II spicules,” was found in high-resolution imaging observations taken at the Ca II H line (De Pontieu et al. 2007b). These structures are more slender (apparent widths  $\approx 1''$ ) and exhibit higher plane-of-the-sky speeds ( $\approx 50$ – $100$  km s $^{-1}$ ) than their “traditional” counterparts.

Chromospheric plages are regions of higher intensity in chromospheric lines (e.g., traditionally in Ca II H & K or in H $\alpha$ ) with stronger magnetic fields as compared to the typical

quiet Sun, but weaker ones if compared to those in a sunspot chromosphere. Therefore, plages can be viewed as areas in the solar chromosphere that are intermediate between sunspots and quiet Sun conditions. In such plage regions we find short and dynamic structures called “dynamic fibrils,” which are driven by slow-mode magnetoacoustic shocks that propagate from the photosphere to the chromosphere and beyond (Hansteen et al. 2006; De Pontieu et al. 2007a; Skogsrud et al. 2016; Carlsson et al. 2019).

The definition of “plage” has never been done strictly; it was—and remains—a loose observational term. Deslandres (1893) first used the term “plage” metaphorically (in French it means “beach” or “seashore”) to help explain his interpretation that such bright regions seen in his early Ca II H and K full-disk spectroheliograms correspond to elevated structures sticking out of the photosphere, in an analogy to sandy beaches emerging from (and appearing brighter than) the ocean.<sup>9</sup> As a result of this loosely defined term that so poetically describes regions with higher intensity of chromospheric lines as compared to those in the typical quiet Sun, early and modern observers have been determining such areas on the Sun with relative freedom: either (a) “by eye,” i.e., by manual definition of the boundaries of a plage region (for a recent example see Carlsson et al. 2015), or (b) in a quantitative manner, i.e., by selecting a certain intensity threshold for a chromospheric image or even an area of moderately intense magnetic fields (e.g., Jafarzadeh et al. 2019 and references therein). With the present paper we raise caution in that the exact method of identifying and isolating a plage from its immediate surroundings (e.g., sunspots, pores, quiet Sun) can introduce statistical biases that can have a significant impact on quantitative comparisons between chromospheric observables (see Sections 3, 4.1.2, 5, and Appendix).

Quantitative comparisons between different observed diagnostics are a key way to study the physics of chromospheric plasmas and to understand the diagnostic power of various chromospheric observables. Recently, the Atacama Large Millimeter/submillimeter Array (ALMA; Wootten & Thompson 2009) has offered its unique capability in producing high-resolution (<1”) and high-cadence (2 s) imaging of free–free emission (from chromospheric electrons) in the millimetric (mm) part of the spectrum.

Under chromospheric conditions the source function,  $S_\lambda$ , of the free–free emission at mm wavelengths is in LTE and so the source function is Planckian,  $S_\lambda = B_\lambda(T)$ . In addition, since the radiation is in mm wavelengths (i.e., low frequencies), the Rayleigh–Jeans approximation holds true, which means that the source function is linearly proportional to the blackbody temperature. This mm emission becomes optically thick over a rather narrow width of heights. Given that, we can measure the “brightness temperature,”  $T_b$ , i.e., the temperature a blackbody would have to match the brightness of the observed emission.  $T_b$  can thus be used to infer the local plasma temperature. The local conditions producing the optically thick free–free emission can originate from quite a wide range of geometric heights. Additionally, the formation height depends on the electron density, which is also expected to vary wildly in the

chromosphere. Conversely, we do not know the exact height where the free–free emission becomes optically thick, and therefore, we do not know where exactly  $T_b$  is measured (Carlsson & Stein 2002; Wedemeyer-Böhm et al. 2007; Loukitcheva et al. 2015; Rutten 2017; Martínez-Sykora et al. 2020b). Rutten (2017) argued that ALMA mm emission should be dominated by fibrils and spicules along the canopy as typically seen in H $\alpha$  or with even higher opacities. In the present paper we take advantage of the high–spatial resolution ALMA observations at  $\lambda = 1.25$  mm and address the formation height problem for this free–free mm emission.

Bastian et al. (2017) presented the first quantitative comparison between UV chromospheric emission and ALMA free–free emission. These authors explored how well the  $T_b$  measured with ALMA at 1.25 mm correlate with the average chromospheric radiative temperatures,  $T_{\text{rad}}$ , inferred by converting the average Interface Region Imaging Spectrograph (IRIS)/Mg II h2v and h2r peak intensities,  $I_\lambda$ , into  $T_{\text{rad}}$  via the Planck function:

$$T_{\text{rad}} = \frac{hc}{k_B \lambda} \frac{1}{\ln\left(\frac{2hc^2}{\lambda^5 I_\lambda} + 1\right)} \quad (1)$$

where  $c$  is the speed of light,  $h$  is Planck’s constant, and  $\lambda$  is the average wavelength position of the Mg II h2v and h2r peaks. This study reported a positive correlation with some scatter mainly attributed to the expectation that  $T_{\text{rad}}$  might not be perfectly correlated with  $T_b$ , since the source function for Mg II h2v/h2r decouples from the local temperature with increasing height in the atmosphere (because Mg II k & h are scattering lines). Similar results were found by Jafarzadeh et al. (2019) using the same ALMA/IRIS observations in Bastian et al. (2018), although they studied correlations between ALMA/Band6  $T_b$  and  $T_{\text{rad}}$  from Mg II for each of its h and k line features individually. da Silva Santos et al. (2020) performed inversions of IRIS observations and used ALMA data as an additional constraint. Apart from several low-temperature regions they found high-temperature regions that seem to be associated with shocks pervading the chromosphere. Wedemeyer et al. (2020) presented ALMA/Band3 interferometric maps and discussed the potential of such observations for the study of the dynamic chromosphere on small scales (such as small loops).

In this study, we composed and analyzed a unique and comprehensive data set from joint observations with ALMA, IRIS (De Pontieu et al. 2014), and the Solar Dynamics Observatory (SDO; Pesnell et al. 2012). Our data set is most appropriate for investigating the rich dynamics of the solar chromosphere and transition region in plages and their peripheral areas—including spicules and chromospheric shocks—thanks to the synergy of the high spatial and temporal resolution of spectral and imaging observations by IRIS with the high-cadence and unique temperature-diagnostic capabilities from ALMA interferometric observations. A companion publication (Chintzoglou et al. 2021, hereafter Paper I) focuses on the evolution of a spicule in the western part of the IRIS raster. Here, using the same data set, we focus on the general structure and the dynamics of chromospheric plages. Since some of our results show discrepancies with those reported by several previous studies, we perform and present a thorough comparison to elucidate the reasons behind the discrepancies.

<sup>9</sup> As it appears, Deslandres introduced the term “plage” to solar physics rather unintentionally, because after a full paragraph of using that term (as a metaphor) he concluded that these bright chromospheric regions shall be named *flammæ faculæres* (i.e., “facular flames,” due to the association with faculae in the photosphere; Deslandres 1893).

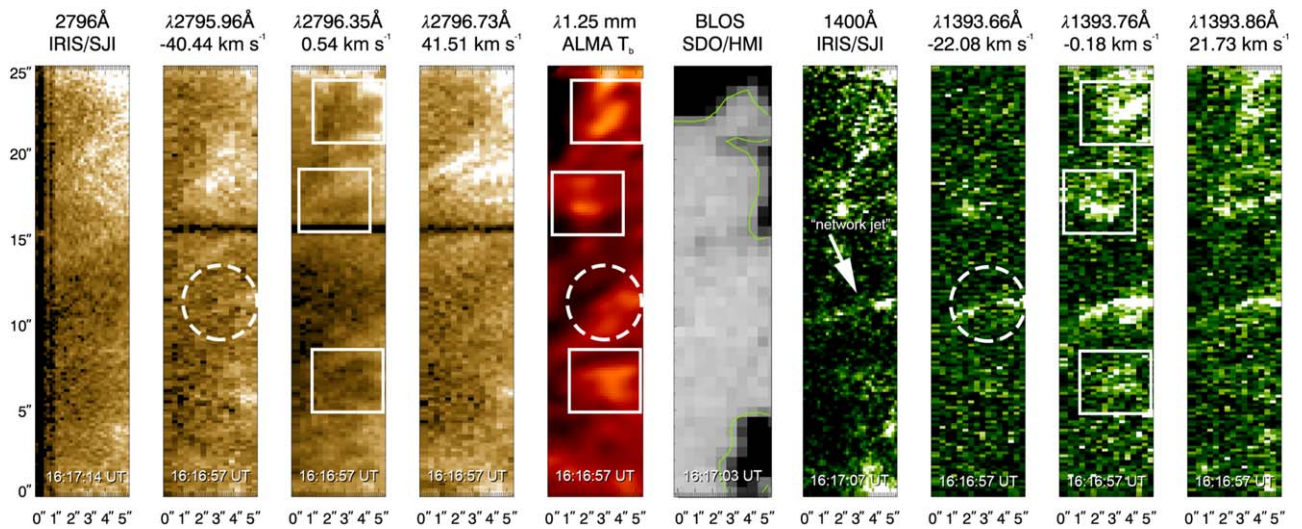


**Figure 1.** Intercomparison of IRIS and ALMA/Band6 observations at an intermediate time in our observing window. Raster scans are shown at selected wavelength positions in Mg II (left panels) and Si IV (right panels) showing the clear appearance of the rapidly evolving structure in Mg II and Si IV (dashed circles). Boxed areas denote locations where intensity features in the Mg II maps appear anticorrelated to those in the Si IV and ALMA/Band6 maps. In the panels with the SDO/HMI magnetogram (scaling clipped at  $\pm 250$  G) we overplot an isocontour of  $\pm 100$  G. The FOV is thus split into two strongly magnetized areas (north and south of the FOV) separated by a weakly magnetized area (in the middle). An animated version of the IRIS and ALMA/Band6 raster scans can be found in the online journal. The animated images provide the same selected wavelength positions of Mg II and Si IV shown in the static figure. The animated version also includes four wider-field panels showing the full IRIS/SJI and ALMA fields. The four additional animated images include (clockwise from top left) the magnetic field distribution from SDO/HMI, the Mg II 2796 Å and Si IV 1400 Å IRIS/SJI full-field images, and the full-field ALMA/Band6 1.25 mm image. These full-field images are annotated with the ALMA (yellow) and raster-scan (white) FOV. The animations run from 15:59 to 16:33 UT on 2017 April 22.

(An animation of this figure is available.)

To carry out this investigation, we introduced a novel empirical methodology to better determine the boundaries of regions of plages in the observations, and we also employed a state-of-the-art numerical model to synthesize observables for comparison with the observations.

This paper is structured as follows: in Section 2 we provide a description of the observations and the model used in this work. In Section 3 we describe our proposed methodology for the determination of pure regions of plages, and in Section 4 we continue with the analysis and presentation of our results, followed by a discussion of the discrepancies in Section 5. We close with a summary and conclusions in Section 6.

## 2. Observations and Modeling

We observed a plage region in the leading part of NOAA Active Region 12651 on 2017 April 22 at heliographic coordinates N11°E17°, or at  $(x, y) = (-260'', 265'')$  in helioprojective coordinates (Figure 1(a) of Paper I). The overall spatial distribution of the plage fields in the target appeared semicircular in shape, as organized around the outer boundary of a supergranule (Figure 1(b) of Paper I). The common IRIS–ALMA field of view (FOV) contained part of that plage, including a photospheric pore (e.g., Figure 1(c) of Paper I). A very high degree of similarity between morphological structures seen in ALMA/Band6 maps and IRIS/SJI 1400 Å images was evident in our observations (Figure 1 of Paper I). We address the origin of this outstanding similarity in Section 4.1. For additional details regarding the reduction of the IRIS and ALMA observations used here refer to Section 2 of Paper I. ALMA captures in ultrahigh cadence (2 s) the dynamics in plages and the interesting evolution of linear-like structures, including indications of shocks in the region of the plage. In this work, we address the nature of the high correlation we found between spatially resolved features seen

in IRIS/Si IV and ALMA/Band6 and in other observables both in the observations and in the model (Section 4.1).

### 2.1. General Morphology of the Dynamic Plage in IRIS and ALMA/Band6 Observations

From a top-level view, the chromospheric intensities in the observables (Figure 1) are brightest in the strongly magnetized regions and dimmer in the interloping weakly magnetized area. Our ALMA/IRIS raster FOV contains plages in the northern and southern parts as well as the outskirts of the plages, i.e., the plage “periphery.” For context imaging and for an image of the overall magnetic distribution in our target region see Figure 1(b) of Paper I. Here, we address the physics of plages and the problem of defining regions of plages. Therefore, we study the full FOV as well as the individual parts in the FOV that are designated as (a) plage and (b) plage periphery (see following sections). Lastly, in Figure 1 we indicate locations of intensity features in Si IV 1392 Å rasters that show outstanding similarities (intensity correlations) to those of ALMA/Band6 (boxed regions). Remarkably, these regions appear to be weakly correlated or are even found in anticorrelation between Mg II 2796 Å rasters and ALMA/Band6. We address the origin of this finding with a rigorous analysis of the observations, and we discuss the physical implications using an advanced magnetohydrodynamic model in Section 4.

### 2.2. Bifrost Simulation of Dynamic Plage and Synthesis of ALMA and IRIS Observables

The simulation analyzed in this paper produced Type II spicules in several locations in the computational domain, between regions of emerging flux and plages (the latter containing dynamic fibrils). Additional details regarding the



simulation and the synthesis of observables can be found in Paper I and in Martínez-Sykora et al. (2020a).

In order to perform a comparison of the physics and the evolution of the observed plage and its periphery with those in the simulation, we focus on two particular regions, (1) a low-magnetic flux “spicule region” at  $x = [40,45]$  Mm (seen to develop at a favorable angle to the line of sight (LOS); Figures 2(a), (b), annotated and indicated with arrows) and (2) a “fibril region” at  $x = [25,35]$  Mm above a stronger flux concentration (containing a dynamic fibril). Thus, regions (1) and (2) represent a plage periphery and a plage region, respectively, appropriate for comparison with our IRIS–ALMA observations of a plage and its periphery near the disk center. The viewing geometry chosen is of an “observer” looking from above down on the domain (i.e., assuming a LOS along the vertical direction in the simulation). In Figure 2 we show spacetime plots (hereafter,  $x-t$  plots) for ALMA/Band6 (panel (c)), Mg II in a wavelength range of 0.7 Å centered at the k3 rest wavelength (2706.35 Å; panel (e)), and Si IV 1393 Å (panel (g)). We assume that the observed spicules are not oriented in such a way that our LOS intersects them perpendicularly over their length, as the latter orientation seems an extreme case (likewise for the case where the spicule is viewed along its axis). Thus, our geometry in the model seems reasonable for the interpretation of the observations.

### 3. An Empirical Method for Determining and Characterizing Areas of Plages

Chromospheric plages could be defined as regions of high chromospheric intensities above magnetic spatial distributions, with magnetic fluxes stronger than those in the quiet Sun but weaker than those of sunspots and photospheric pores. An observer can determine such areas either (a) by eye and by cutting out a region manually (e.g., Carlsson et al. 2015) or (b) in a quantitative manner, i.e., by selecting a certain intensity threshold for a chromospheric image or even an area of moderately intense magnetic fields. However, since we are interested in quantitative comparisons between different observables in plage regions, care must be taken to exclude features that are not classified as plages. Thus we should exclude (i) photospheric pores, which may often form sporadically in plages by random convergence of unipolar magnetic fields, and (ii) dark fibrils or other small and cool filamentary structures often seen in the vicinity of sunspot penumbras/superpenumbras. Therefore, in the present study we consider a plage to be a hot magnetic canopy above photospheric magnetic concentrations. Additionally, we have been cautious to exclude other features, such as pores or the superpenumbra from nearby spots. We have been cautious to not include other elements, such as pores or the superpenumbra from nearby spots.

Flux-segmented (or thresholded) magnetograms were produced by clipping values at  $\pm 0.1$  kG to distinguish between strongly and weakly magnetized areas. We used the segmented magnetograms as a visual guide to aid the determination of plages in our chromospheric observables. This confirms that the FOV is naturally split into two distinct plage regions (one north and one south of the FOV) separated by a weakly magnetized region in the middle. With this in mind and given (i) the several linear-like structures (and spicules; see Paper I) present in that quieter area, (ii) the small size of the raster along the  $x$ -direction ( $5''$ ), and (iii) the knowledge that plages and

magnetic fields reside in the west just outside the raster FOV (Figure 1(b) of Paper I), we conclude that this middle region is part of the periphery of the same plage. We also note that the entire plage is at a Sun-center angle of  $\approx 20^\circ$ . Here, our common ALMA/IRIS FOV contains just the eastern boundaries of this plage region. This simplifies our task in determining the true chromospheric boundary of our plage on only one side. However, we caution of possible systematic geometric offsets between the boundaries of extended plage regions, e.g., if they are defined in the photosphere (via thresholded magnetogram maps) and used to describe the boundaries of the higher-lying chromospheric plage area.

We inspected imaging in the continuum from IRIS/SJI Mg II 2832 Å, which clearly shows the existence of a photospheric pore within the northern part of the plage in the common IRIS–ALMA FOV. The pore is persistent for most of the IRIS–ALMA/Band6 co-observations. Here we caution that excluding the pore from the chromospheric plage pixels with the use of a threshold on the magnetogram maps is not a straightforward task. A pore’s area determined at the photosphere is likely a smaller area than the pore’s associated area at chromospheric heights due to lateral expansion/“fanning” of the pore’s magnetic field with height. To properly remedy this issue, we employed ALMA/Band6 maps segmented at a low threshold  $T_b \geq 6500$  K. This approach effectively removed the chromospheric counterpart of the pore in the plage.<sup>10</sup> The final result from the application of our method can be seen in the top panel of Figure 3, where we overplot on the SDO/HMI map regions of the plage within a red contour and with orange contours show the excluded area above the pore region. The plage periphery is the area within the blue contour, where linear-like structures and spicules are seen to develop against a significantly darker (and quiet Sun–like) background (see Paper I).

We summarize here the observational quantities and requirements for defining plages:

1. photospheric magnetogram to be used as a guide (threshold choice of  $\pm 0.1$  kG, although similar results can be found for even lower thresholds)
2. continuum maps to properly identify areas of pores within plages or sunspot penumbras
3. chromospheric intensity maps (e.g., Mg II or any other chromospheric observable) to remove pores with proper intensity thresholds above the identified regions of pores
4. avoiding the vicinity of well-developed sunspots, i.e., regions of the sunspot superpenumbra that typically extend further out than the sunspot penumbra.

By carefully considering these criteria we can determine “clean” regions of chromospheric plages. As we show in the following paragraphs, when these are not taken into consideration simultaneously, sources of bias appear that lead to discrepancies between our results and previous studies.

<sup>10</sup> We note that any of the Mg II, Si IV, or C II raster maps from IRIS could be used equally well to remove the chromospheric counterpart of the photospheric pore for a choice of threshold. However, since ALMA/Band6 maps are produced with an irregular resolution element, i.e., the so-called “beam,” here we make a mask from Band6 to further restrict the accidental inclusion of lower  $T_b$  values in our comparisons due to spatial smearing from the beam.

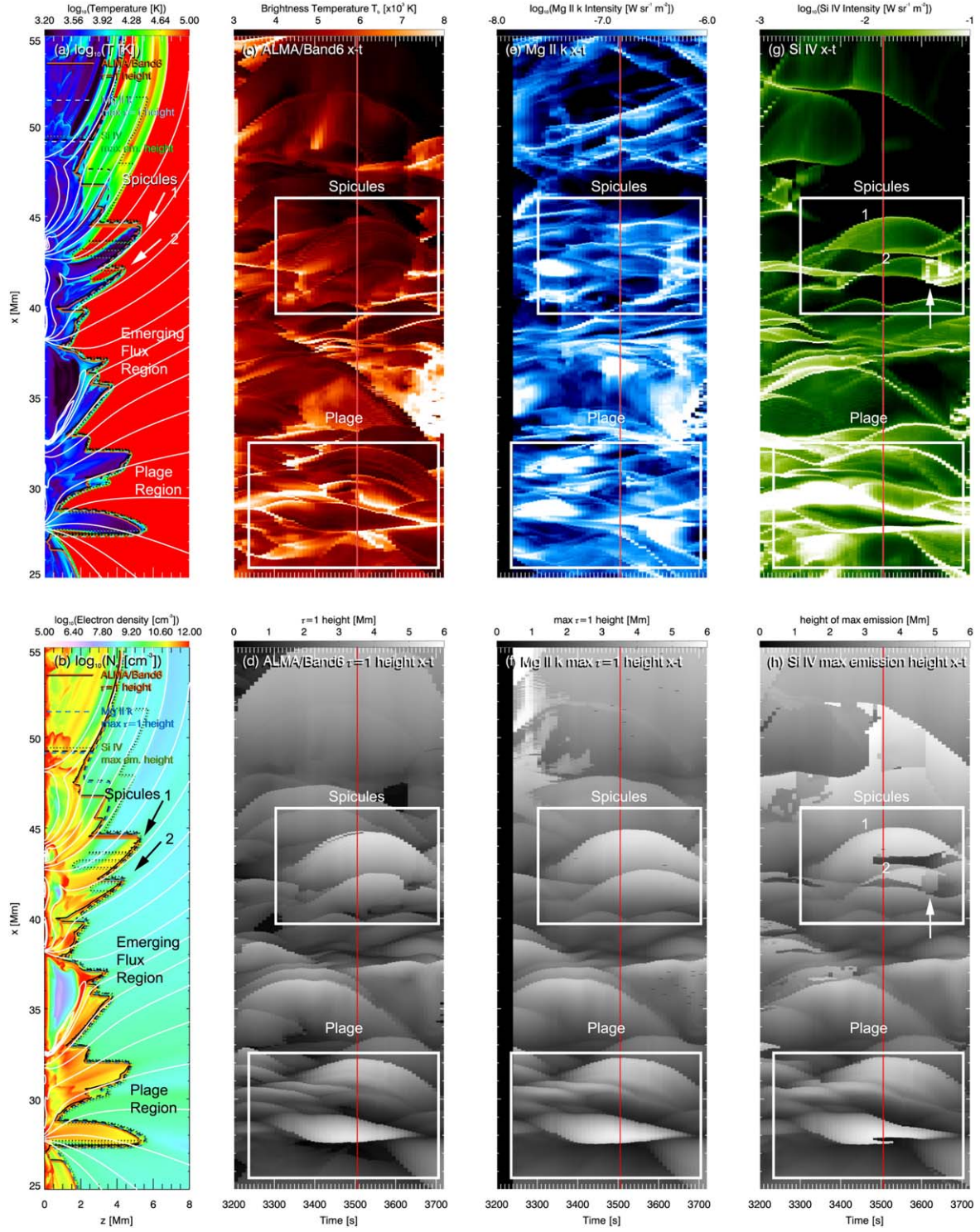


**Figure 2.** Synthetic  $x-t$  plots from the Bifrost simulation. The leftmost panels show snapshots from the simulation at  $t = 3500$  s for (a)  $\log_{10} T$  and (b)  $\log_{10} N_e$ . Upper panels (c), (e), and (g) show  $x-t$  in ALMA/Band6  $T_b$  (in red), Mg II k (in blue), and Si IV (in green) synthesized intensities, respectively. Bottom panels (d), (f), and (h) present  $x-t$  plots for the geometric height, with  $\tau = 1$  for ALMA/Band6, the maximum  $\tau = 1$  height for the wavelength-integrated Mg II k, and the height of maximum emission for Si IV. Boxed areas denote regions of spicules (best seen in Si IV) and plages. With a red line in the  $x-t$  plots we mark the time shown in panels (a), (b). An animation of the  $\log_{10} T$  and  $\log_{10} N_e$  simulation images is available in the online version of the journal. The animation runs for 500 s of the simulation (3200–3700 s). The same  $x-t$  plots in the snapshots are shown in the animated simulation images, except that the Si IV maximum emission is replaced with the ALMA/Band6 + Mg II–Si IV spacetime plot. The spicule regions are not annotated in the animation.

(An animation of this figure is available.)



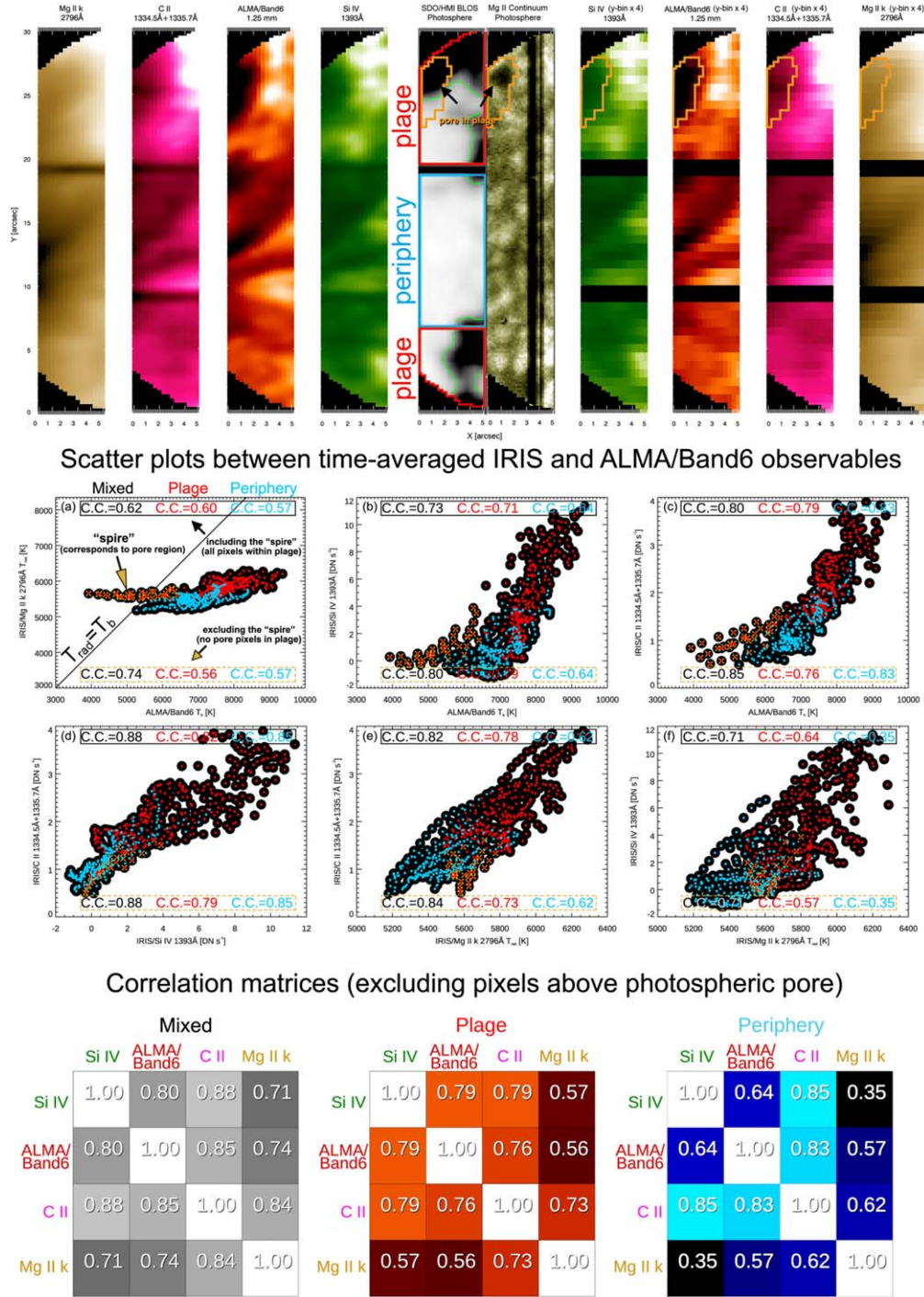


**Figure 3.** Top panels: Time averages of Mg II k ( $T_{\text{rad}}$ ), C II, and Si IV from IRIS and ALMA/Band6 ( $T_b$ ) together with their 4 pixel binned version along the slit (y-axis). In the middle we show the time-averaged LOS magnetogram (green contour at  $\pm 100$  G) with the subregions considered in the correlation plots (red = plage, blue = periphery of plage) and a Mg II 2832 Å SJI map showing the presence of a photospheric pore in the plage region. Orange contours show the pixel area determined relative to the pore, which is excluded from our analysis. Middle panels (a)–(f): Scatter plot for each combination of the 4 pixel binned average series. Correlation coefficients (C.C.) are given for (i) points inside the plage area (shown in red), (ii) points inside the area containing the periphery of the plage (blue), and (iii) the entire FOV (black) with and without the pixels in the pore region (top and bottom groups of C.C. values, respectively). Note the significantly high correlation between ALMA/Band6 and C II and Si IV. Bottom panels: C.C. values excluding the pore pixels organized in correlation matrices. See text for detailed discussion.

## 4. Analysis and Results

### 4.1. Understanding the Origin of the Similarities between ALMA/Band6 and IRIS Observables

The high degree of similarity between the ALMA/Band6 and Si IV observables is illustrated in Figure 1. In that figure we

point to locations in the FOV where ALMA/Band6 emission appears in anticorrelation with Mg II k intensity patterns (boxed areas in rasters of Figure 1). Here we perform a quantitative analysis of the degree of similarity between ALMA/Band6 and other chromospheric and transition-region observables from IRIS to better understand and constrain the diagnostic potential

of ALMA/Band6 as a tool for measuring the temperature of chromospheric plasmas. As we mention in Section 1, the actual formation height of ALMA emission is not well known. In particular, to link this work with previous studies, we first carry out the analysis using (a) observables time-averaged over the entire time series (Section 4.1.1), and we discuss discrepancies with previous studies. Then we use (b) observables without averaging in time to also consider the time evolution (Section 4.1.3). We then follow this with the results of our analysis from the model by considering both the time evolution and the height–wavelength dependence of the IRIS observables (Section 4.1.4).

#### 4.1.1. Quantification of Morphological Similarities between Observables Time-averaged over the Entire Image Series

Here, we perform an intercomparison between wavelength-integrated rasters in Si IV 1393 Å, C II 1335 Å, Mg II k 2796 Å, and ALMA/Band6.

Comparison between the optically thick observables ALMA/Band6  $T_b$  and Mg II is typically done with Mg II expressed as radiative temperature,  $T_{\text{rad}}$ , in units of temperature [K]. Previous studies (e.g., Bastian et al. 2017, 2018; Jafarzadeh et al. 2019) have found that the intensity of Mg II k2 or h2 peaks correlates with mm emission from ALMA/Band6 observations, supporting the expectation that ALMA/Band6 emission forms at mid to low chromospheric heights. To compare our study with previous work we performed double Gaussian fitting (Schmit et al. 2015) for the Mg II raster data and produced maps representing each feature of the k and h lines, i.e., k2v, k2r, h2v, h2r, k3, and h3. We computed  $T_{\text{rad}}$  with Equation (1) for each of these maps. We also considered the wavelength-integrated Mg II k quantity we produced and used in the previous sections via Equation (1) and obtained  $T_{\text{rad}}$  at each wavelength position of the rasters separately (within a range of  $\Delta\lambda = 0.7$  Å from the line center). We then produced the average quantity of  $T_{\text{rad}}$  representing the wavelength-integrated Mg II k data, by taking the average of  $T_{\text{rad}}$  produced in that range. This choice of  $\Delta\lambda$  offers the benefit of including all line features of Mg II k (i.e., k2v, k2r, and k3) without extending too much into the line continuum.

For the wavelength-averaged optically thin observables, computing  $T_{\text{rad}}$  is physically meaningless. We keep the observed values expressed in arbitrary intensity units [DN s<sup>-1</sup>]. For Si IV, the integration was performed for each frame in these rasters in a wavelength range of 0.2 Å. In order to increase the signal-to-noise ratio (S/N) in the C II raster we summed both lines (centered at 1334.5 Å and 1335.7 Å) and then integrated the sum in wavelength over 0.2 Å. The C II (not always optically thick, so we keep it in [DN s<sup>-1</sup>]) rasters suffer from low counts, making the presence of hot pixels more impactful in the statistics, with plenty of hot pixels visible in the map from the average C II image series. We determined that the hot pixels can be extracted easily, since their values exceed the values from persistent structures owing to real C II signals. Thus, at each frame, we removed any hot pixels exceeding 10 DN s<sup>-1</sup> and substituted the resulting missing-pixel values via linear interpolation from the values of immediately neighboring pixels. While significant noise was still present in each frame due to low photon counts, inspection of the time-averaged map before and after the removal of hot pixels showed that the S/N was improved satisfactorily.

A common approach in multiwavelength studies utilizing data from different observatories/instruments is to ensure that any time differences in the image series between different observables are (1) properly matched/synchronized and (2) small enough and appropriate for addressing particular science questions. Both are required to effectively “freeze in time” the plasma evolution between all the different wavelengths. This becomes a serious concern in studies of the highly dynamic chromosphere, such as the one we report in the present work. Here, we match our ALMA/Band6 2 s cadence series by composing “rasters” that match the time of each slit sampling position to within  $\pm 1$  s. We also performed the analysis presented here by selecting the frame at the time corresponding to the middle of each raster scan (raster cadence of 26 s, resulting in a  $\pm 13$  s time difference) but found no significant change in our results (i.e., of the order of  $\sim 1\%$ ). This presents an improvement as compared to previous studies (e.g., Bastian et al. 2018; Jafarzadeh et al. 2019), where the minimization of time differences was limited due to the data series used, resulting in a highly variable time matching between ALMA–IRIS observables (i.e., 0.5–2 minutes). In particular, Jafarzadeh et al. (2019) acknowledged that significant evolution may be ongoing during this period of time between the sampling of the ALMA–IRIS observables, and also reported findings by a separate analysis where the time difference was strictly chosen to be 0.5 minutes (marginally improving agreement between ALMA–IRIS observables). Here, with a maximal difference of  $\pm 1$  s we “freeze” the plasma evolution consistently and successfully between each observable over our entire ALMA–IRIS image series. However, since the C II rasters have low photon counts, in this subsection we restrict the comparison between time-averaged rasters over the entire IRIS–ALMA/Band6 common time series (for a time-dependent study of ALMA/Band6 and IRIS Mg II k and Si IV see Section 4.1.3).

To perform a fair comparison with ALMA/Band6, we degraded the wavelength-integrated IRIS raster maps by convolving them with the Band6 beam size and respective position angle at each time frame of our series. Finally, we applied 4 pixel binning along the slit direction for each observable to additionally increase the S/N. The resulting Band6 beam-degraded and time-averaged IRIS maps (before and after 4 pixel binning) are shown in the top panels of Figure 3. In the panels before binning (top left) we can see some cosmetic artifacts, namely a dark line due to the fiducial point that blocks the light in the slit, in addition to a linear-shaped intensity depression (mostly seen in the far-UV (FUV) observables), which appears similar to the shadow produced by the fiducial point. In our analysis, we masked out and excluded these two rectangular areas (see dark bands along the  $x$ -direction in the 4 pixel binned maps).

#### 4.1.2. Quantitative Comparison between Time-averaged Observables in Plage and Its Periphery

At first sight, the similarity between C II and ALMA/Band6 is striking. We proceeded by calculating the linear C.C. (Pearson  $r$ ) between each of the four observables (i) inside the plage region, (ii) inside the region containing the periphery of the plage, and (iii) for the full FOV in the rasters mixing the plage with its periphery, first with the pore (the respective C.C. value for each region is shown within a black box at the top of each scatter plot). Then we also calculated the C.C. for regions (i) and (iii), after the pore area was excluded in each of the



observables (values shown within the dashed orange box in each scatter plot; region (ii) is obviously unaffected by the removal of the pore pixels). The inclusion of this low-temperature ALMA/Band6 region in the calculation of the C.C. for the plage and for the full FOV can be readily seen to influence the values presented in the scatter plots in Figures 3(a)–(c). The pixels in the region above the pore produce a clear “spire”-like feature or a “tail of points” toward low ALMA/Band6  $T_b$  values ( $4000 \leq T_b \leq 6500$  K, i.e., our  $T_b$  threshold choice for producing the pore mask is fully consistent with representing this feature). Removing those pixels with the application of the pore mask improved the C.C. for the full FOV and plage significantly (red points marked with an orange “x” symbol). However, we caution that the C.C. obtained over the full FOV led to different results since it mixed plage regions with much quieter regions in the plage periphery, i.e., regions with very different physical conditions.

We first focus our analysis and discussion on the plage (excluding the pixels above the photospheric pore) and periphery regions separately and save the analysis of the full FOV as a way to link our work to previous studies. To facilitate the presentation of the results, in the bottom panels of Figure 3 we organize the various C.C. values obtained from each combination of the observables with the aid of correlation matrices. The correlation matrix for the plage shows that C II is highly correlated with all other observables (C.C. within 0.73–0.79). In contrast to that, the observable with the lowest correlation with observables in the plage is Mg II k  $T_{\text{rad}}$ . ALMA/Band6, Si IV, and C II form a triad with the highest C.C. Perhaps this should not be a surprise, since these high values are fully consistent with Si IV and ALMA/Band6 forming close to each other, thus probing similar structures. In addition, we emphasize that Mg II  $T_{\text{rad}}$  is averaged over 0.7 Å, so that it mixes information from a wide range of heights. We note that if we had used the wavelength-averaged Mg II k time-averaged map expressed in intensity [DN s<sup>−1</sup>] instead of  $T_{\text{rad}}$  in [K], our results in the correlation study we present here would not have changed beyond a few percent. In addition we emphasize that if we had imposed thresholded magnetogram masks for the plage areas, the results would not have changed beyond 3%–5%, which further confirms the robustness of our methodology described in Section 3.

The similarity between C II and Si IV has been mentioned previously in visual comparisons between IRIS C II, Si IV, and Mg II rasters (e.g., Rathore et al. 2015a). In a study by Rathore et al. (2015b, e.g., Figure 17 therein), Si IV was found to form consistently higher (having normally a formation height in the transition region, at  $T \approx 80,000$  K) than Mg II and C II, although C II was found to form at heights either above or below those of Mg II k3. However, it was also noted that C II primarily forms above the formation height of Mg II.

Our results in the correlation matrix for the plage (Figure 3) support this finding, given that C II shows very high correlation with ALMA/Band6 and Si IV, the latter being understood as all these observables having formation heights relatively close to one another, effectively sampling the conditions along similar parts of structures above the plage. Mg II k  $T_{\text{rad}}$  seems poorly correlated with all other observables but C II, suggesting that C II forms above Mg II k but between Mg II k and ALMA/Band6 and Si IV. To this we should add that the interesting anticorrelation seen between the maps of Mg II k and ALMA/Band6 and Si IV in certain locations of the FOV (Figure 1;

boxed regions in plage), presumably due to enhanced absorption, may have the effect of weakening the correlation of Mg II k with the other observables.

The correlation matrix for the periphery of the plage shows a similar picture. The C.C. between C II and the other three observables remains the highest as compared to any other combination of three (out of four) observables. The significant strength of the correlations with C II for the periphery appears consistent with the results of Rathore et al. (2015b), which place the formation height of C II higher than that of Mg II and thus closer to that of Si IV in the fibril regions (Figure 18 therein). Note, however, that Rathore et al. (2015b) did not average Mg II k over 0.7 Å. The periphery of the plage here contains several linear-like structures, which are of similar geometry to the simulations shown in Rathore et al. (2015b; e.g., see in our Figure 3 the persistent thread-like structures in the time-averaged maps). On the other hand, this region also exhibits low signals in Si IV and ALMA/Band6. This may explain the significantly lower correlation between Mg II, Si IV, and ALMA/Band6 as compared to that in the plage, since Mg II intensity seems more diffuse in that region. For completeness, we also note here that a study of correlations between C II  $T_{\text{rad}}$  and ALMA/Band6  $T_b$  has been performed by Jafarzadeh et al. (2019), who also found a high Pearson C.C. of 0.83, although it was mentioned there that the origin of this high correlation with ALMA/Band6 is not known.

Since our results are in contrast with those of previous studies, we further discuss the reasons behind the discrepancies in a separate paragraph (Section 5).

#### 4.1.3. Time-dependent Quantitative Study of Morphological Similarities between Observables

We note that during the time range of co-observations with ALMA/Band6, significant evolution was ongoing over the entire FOV. To get a clearer picture and to assess the similarities by considering the dynamic evolution in the common FOV, we further focus this analysis on Si IV and Mg II, which, thanks to the higher photon counts, can be used to explore correlations with ALMA/Band6 at each time step of our comprehensive data set.

In order to determine which regions in the common IRIS–ALMA FOV exhibit high morphological similarities between our set of observables, we split the FOV in subregions, or “correlation bins,” and we measured the C.C. between the different observables at each time step of our series. In the top panels of Figure 4 we show the size of the correlation bins on time-averaged, wavelength-integrated maps degraded with the ALMA/Band6 beam and position angle. Furthermore, we distinguished the sign of the C.C.—positive C.C., denoting a positive correlation of the intensities, and negative C.C., representing anticorrelation. The latter would allow us to locate when and where such anticorrelation between (1) Mg II k and (2) either Si IV or ALMA/Band6 occurs. The time evolution of the C.C. per bin is presented in the form of time plots in the bottom panels in Figure 4. For reference, we also show time plots of the average time evolution within the correlation bins for each of the observables as average intensity per bin. Note that for the calculation of the C.C. per bin per time step we did not perform spatial averaging, and we used all the individual pixels within each correlation bin at each time step. Also note that we degraded the IRIS observables with the ALMA/Band6 beam size and position angle.



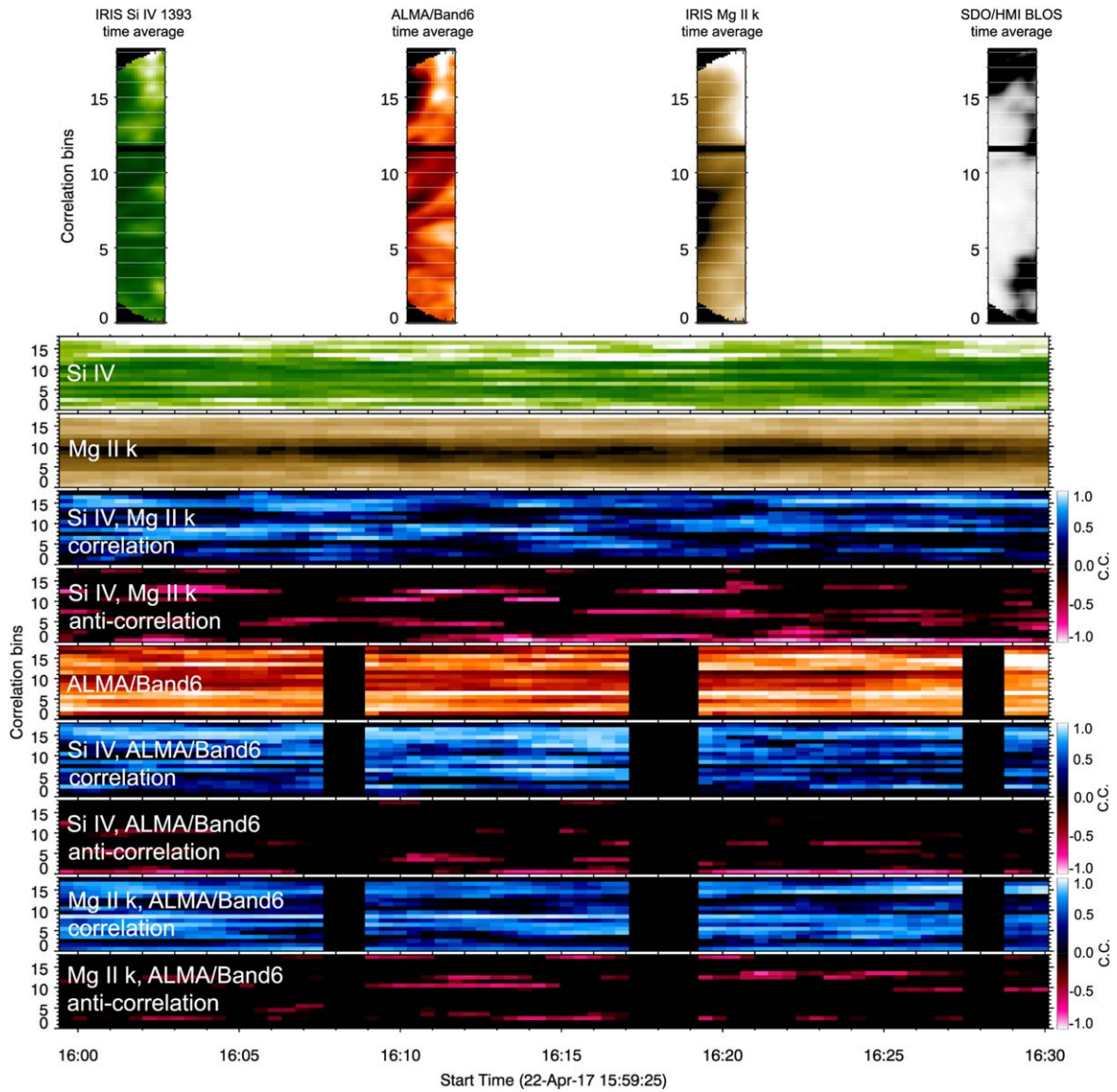


**Figure 4.** Time evolution of correlation and anticorrelation between Mg II, ALMA/Band6, and Si IV. The common FOV (covering the center of the ALMA/Band6 FOV) is segmented into 18 subregions (correlation bins) covering both magnetic and nonmagnetic regions (illustrated with time-averaged maps; top panels). Note that the IRIS image raster series has been degraded with the ALMA/Band6 beam size and position angle at each individual frame. Bottom panels: For illustration purposes we show the bin-averaged  $x - t$  plot for Mg II k, ALMA/Band6, and Si IV 1393 Å. Note the clear distinction between areas of moderate to high correlation and those of anticorrelation between Mg II k and Si IV 1393 Å. Note the very high degree of correlation between Si IV 1393 Å and ALMA/Band6 across all correlation bins and the more sporadic distribution of correlation for Mg II k.

The resulting time plots in Figure 4 vividly highlight the similarities and the differences between the observables. As before, the raster series is integrated along the wavelength centered on each line’s rest wavelength. Remarkably, the FOV of Mg II k and Si IV is split in locations of positive correlation and anticorrelation, confirming our initial visual determination of some locations of anticorrelation between these two observables (e.g., Figure 1; boxed regions in rasters). In addition, at times, there are certain locations where there is strong correlation between the intensities of Mg II k and Si IV, such as the region containing the periphery of the plage with linear-like structures and Type II spicules. However, the most remarkable finding is the sporadic correlation (in terms of both intensity and time persistence) of ALMA/Band6 with Mg II k and the very high and more persistent correlation between ALMA/Band6 and Si IV across the entire FOV, with only a

few instances of anticorrelation. Mg II k is found to be in anticorrelation with ALMA/Band6 in several locations in the FOV. The strong correlation between ALMA/Band6 and Si IV suggests that the spatial extent of bright features—as projected on the plane of the sky—is similar between these two observables, supporting the observation that the geometric heights of the line formation of ALMA/Band6 and Si IV are similar.

Conversely, Mg II k and ALMA/Band6, even though they are nominally expected to have similar plasma temperature sensitivity, appear to sample different geometric heights in the solar chromosphere. This finding is consistent with the synthetic data from the model (Figure 2). Previous work (e.g., Bastian et al. 2017) has considered that ALMA/Band6 forms at the midrange of Mg II formation heights, but as we show later (Section 4.1.4) this does not appear to be the case for

our data set. This is also supported by our study of time-averaged observables in the previous subsection (Section 4.1.2). Note, however, that we use wavelength-averaged rasters, and by averaging in wavelength we find the diagnostic information regarding the formation height of the Mg II k line is biased to lower heights as only Mg II k3 forms at the top of the chromosphere. In fact, in the Mg II k  $x - t$  plot for  $\tau = 1$  of Figure 2(f) for the maximum geometric height, we find a good match with geometric heights for ALMA/Band6  $\tau = 1$ . However, Mg II k3 forms due to absorption, and thus, rasters in k3 capture the maximum absorption in that line. It is therefore our expectation that when Si IV and ALMA/Band6 show emission in dynamic plage structures (or spicules), Mg II k3 (which would be closer to ALMA/Band6 heights) has low intensity due to enhanced absorption. This can lead to anticorrelation with other observables. We address this in the next section (Section 4.1.4).

For completeness, we perform this analysis on the synthetic observables produced from our model. In this case, since the simulation is 2.5D, the synthetic observables can be likened to a “sit-and-stare” IRIS observation, capturing the evolution across a “static 1D slit.” In Figure 5 we show the results. In the top panels we show how we split the domain into correlation bins (here, the bins are essentially 1D, arranged along the simulation domain’s  $x$ -direction at each time step). As in the previous sections, the data have been degraded from the simulation’s scale size, 14 km (grid point) $^{-1}$ , via Gaussian convolution to adopt the nominal spatial resolution of IRIS rasters (0.16 pix $^{-1}$  along the  $y$ -direction) and ALMA (degraded with the Band6 maximum beam size of 0.8). Then we further degraded the synthetic IRIS data by convolving the ALMA/Band6 beam size. In addition, we masked out the location of emerging flux, which effectively separates the “spicule region” at the top of the FOV from the “plage region” at the bottom. The photospheric  $B_z$  shows significantly higher magnetic field strength for the plage region than for other locations of the domain (i.e., of the order of  $\approx 100$  G). Since we use the same correlation bin width in the observations in Figure 4, only a few bins cover the domain in these time plots. However, qualitatively, we get the same picture as before.

In Figure 5 we highlight the region of spicules with a solid ellipse, and we use a dotted ellipse for the plage. For Mg II k and Si IV we see primarily anticorrelation for the plage region (compare the PC1 dashed ellipse with the solid PA1) and an alternation of correlation and anticorrelation for the spicule region (compare solid ellipses SC1 and SA1). The latter seems consistent with Figure 4, where the plage regions in Mg II k and Si IV are more anticorrelated and a more intermixed correlation/anticorrelation is shown for the plage periphery/spicule region (i.e., the anticorrelation plot in the observations shows less strong anticorrelation as compared to the plage regions north and south of the raster’s FOV). For ALMA/Band6 and Si IV we primarily see strong correlation for the plage (Figure 5; compare dotted ellipse PC2 with PA2) and some alternation between correlation and anticorrelation (with clear correlation during the time of the network jet, after  $t = 3600$  s) for the spicule region (compare areas of solid ellipses SC2 and SA2). Lastly, for Mg II k and ALMA/Band6, we see anticorrelation for the plage region (compare PA3 with PC3) but a somewhat sporadic occurrence of correlation for the plage periphery/spicule region (compare areas in solid ellipses SC3 and SA3; there is also positive correlation during the time of

the network jet) intermixed in areas of anticorrelation, again in general agreement with the previous comparison between ALMA/Band6 and IRIS observations (Figure 4).

#### 4.1.4. Explaining the Morphological Similarities in the Synthetic Observables

In order to understand this interesting correlation in the observations we explore the time evolution in the emission and formation height of the synthetic observables for the region with spicules and plages (Figures 6 and 7, respectively; also see Paper I for a detailed analysis of the Type II spicule). For our discussion here, we select three representative time steps along the evolution of a region with spicules and plages in the simulation. In addition, we select three wavelength positions for Si IV and Mg II k (taken in velocity space at  $-13$ ,  $0$ , and  $+13$  km s $^{-1}$  from the line cores). By doing so, we capture the wavelength dependence of the formation height of Si IV and Mg II k during the ascending and descending phases of the spicule’s evolution (see also Figure 8 in Paper I). At each time shown in Figures 6 and 7 we provide a wavelength-space plot (hereafter, “ $\lambda - x$ ”) for Mg II k (i.e., a full spectral profile along the different positions in the simulation domain), which adds relevant information in support of our interpretation presented in this subsection.

At the ascending phase of spicule 1 ( $t = 3350$  s in Figure 6, position  $x = [42, 44]$  Mm; spicule 2 has not started forming yet) we get emissivity in Si IV delineating the spicular column at the blue wing ( $-13$  km s $^{-1}$ ; panel (a); dark green to white color outlining spicule 1), which closely corresponds to the height of ALMA/Band6 emission (shown with dark red to white color in all panels). At the same time, in the area where spicule 2 would eventually develop (position  $x = [40, 42]$  Mm) we can see significant Mg II k intensity in the blue wing (plotted at  $\tau = 1$ ; Figure 6(a)). In Figure 6(d) we show the  $\lambda - x$  plot for this time with the Mg II k spectrum at each  $x$ -position of the domain, with clear rapid blueshifted excursion signatures in the location of formation of spicule 2. Also, in the blue wing of Si IV (Figure 6(a)) we see a front at the tip of the structure delineated by Mg II k intensity (heights around  $z = 2.7$  Mm). This is consistent with the effects of traveling shock waves in the chromosphere before the full development of a spicule.

At the intermediate time step shown in Figure 6 ( $t = 3580$  s; middle column), spicule 2 has fully developed and has almost reached its maximum elongation ( $z = 5$  Mm from the photosphere); most of the Si IV emissivity now comes from the rest wavelength of the line (panel (f); dark green to white color outlining spicule 2). Similarly, at the time of maximum elongation, ALMA/Band6 emission delineates the body of spicule 2 (note the close matching of the geometric heights of line formation between ALMA/Band6 and Si IV; dashed ovals along spicule 2). The spectral profile of the optically thick Mg II (Figure 6(h)) shows that k3 (“dark lanes” in the  $\lambda - x$  plot highlighted with white dotted lines) has shifted to different wavelength positions across the spicule (e.g., panels (f), (g)), and the respective geometric height of  $\tau = 1$  at those different wavelength positions delineates different parts of the spicule (see dashed ovals in panels (f), (g)). In fact, the spicule in Mg II appears as a dark feature (as compared to other locations in the domain), since the line is in absorption. This is either due to the increased opacity or due to the lower source function.

In the last time step shown here ( $t = 3620$  s), spicule 2 has already begun to recede, and the occurrence of network jet



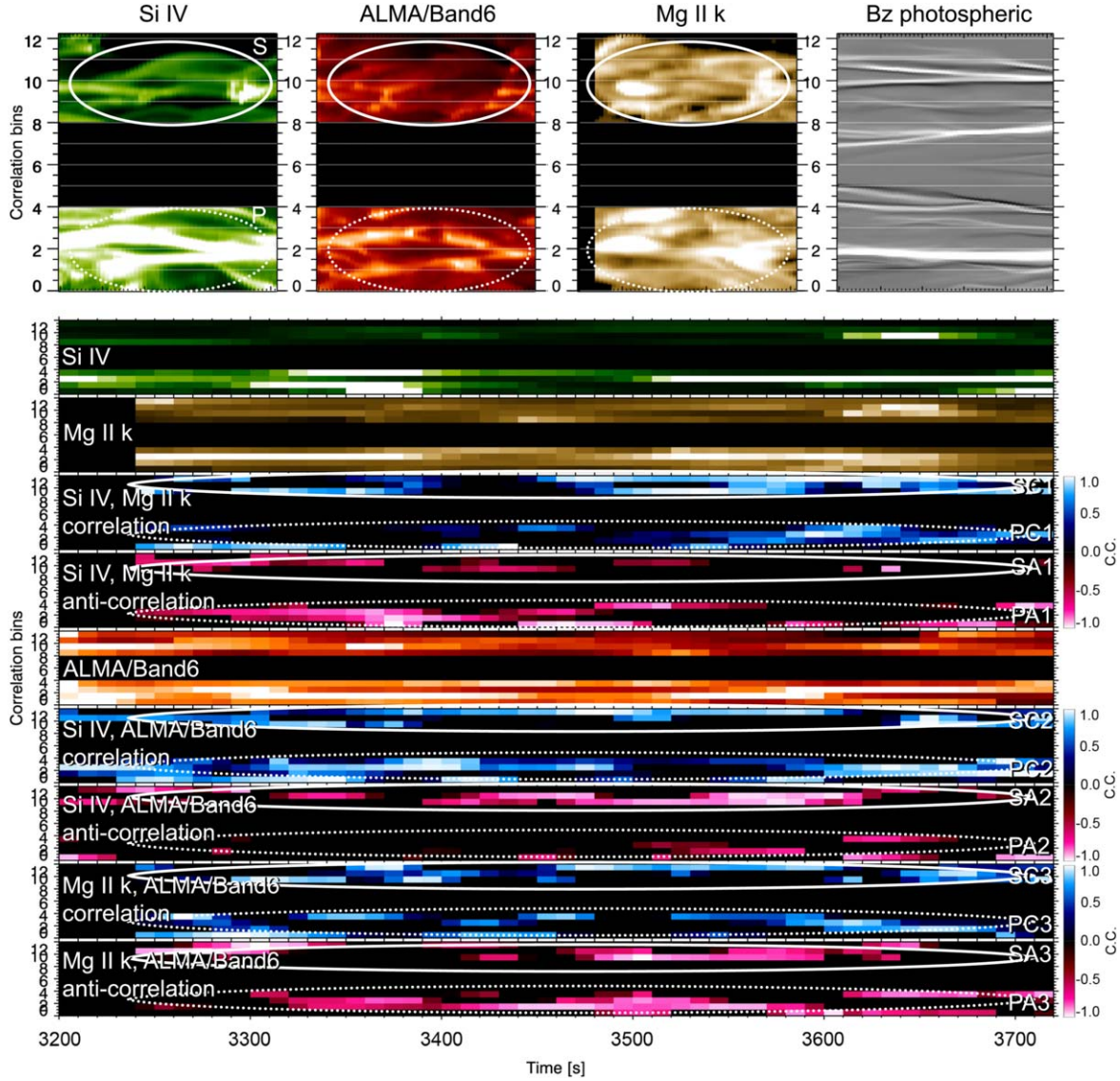


**Figure 5.** Same as Figure 4 but with the analysis method applied to the synthetic observables from the simulation. The spatial resolution in the IRIS–ALMA synthetic observables was degraded accordingly to match the resolution of each observatory, and then IRIS was degraded to match ALMA (with an average ALMA/Band6 beam size of  $0''.8$  along the  $y$ -direction; the  $x$ -direction is the time). The correlation bins have physical widths across the  $y$ -direction similar to those in Figure 4. The emerging-flux region is masked out (blank space), virtually isolating a region of spicules (top region) from a plage region (bottom region). Note the significant spatial extent of persistent anticorrelation between the synthetic Mg II k and ALMA/Band6 observables.

brightening along the spicule strongly enhances the emission in Si IV at the core and in the red wing (panels (j), (k)). The impulsive heating of the plasma in the spicule is so intense that it forces ALMA/Band6 emission to come from lower heights where the plasma is cool enough (the spicule’s height seen in ALMA/Band6 effectively drops from  $z \approx 5$  Mm to  $z \approx 3$  Mm; shown with arrows in panel (j)). At the same time, while significant intensity in Mg II k emanates from low geometric heights (dashed ovals at  $z = 1$ – $1.5$  Mm; panels (i), (j)) at the blue wing and line core, the Mg II k  $\tau = 1$  height in the red wing (panel (k)) is much greater. There, we can see that Mg II k  $\tau = 1$  roughly traces the length of the spicule, albeit at low intensity as compared to other locations with lower geometric heights (note that the same intensity range is used for each of the panels). This again is a manifestation of increased absorption. Here, Figure 6 (panel (l)) reproduces this behavior during the time of the network jet (indicated by an arrow in that panel).

The simulation captures clearly that the high correlation between spatially resolved structures seen in ALMA/Band6 and Si IV is primarily due to the fact that the respective emissions emerge from similar parts of the same structure, both largely delineating the spicular column. Therefore, when observed at the plane of the sky (looking from the top of the simulation domain in this case or, in similar LOSs, for example, off the vertical), the spicule would manifest in both said observables, and the high-intensity features would show up largely as spatially correlated. We cannot say the same, however, for Mg II k, as the  $\tau = 1$  geometric height varies at different wavelength positions. However, we note a characteristic trend: during the ascending (descending) phase of the spicule, the  $\tau = 1$  height at the blue (red) wing roughly delineates the spicule, albeit as a dark structure. There is also the following possibility: if the viewing angle (LOS) was tilted, say, by  $30^\circ$  off the vertical toward small  $x$  (left side of the domain shown in Figures 6(j), (k)), we would be seeing this

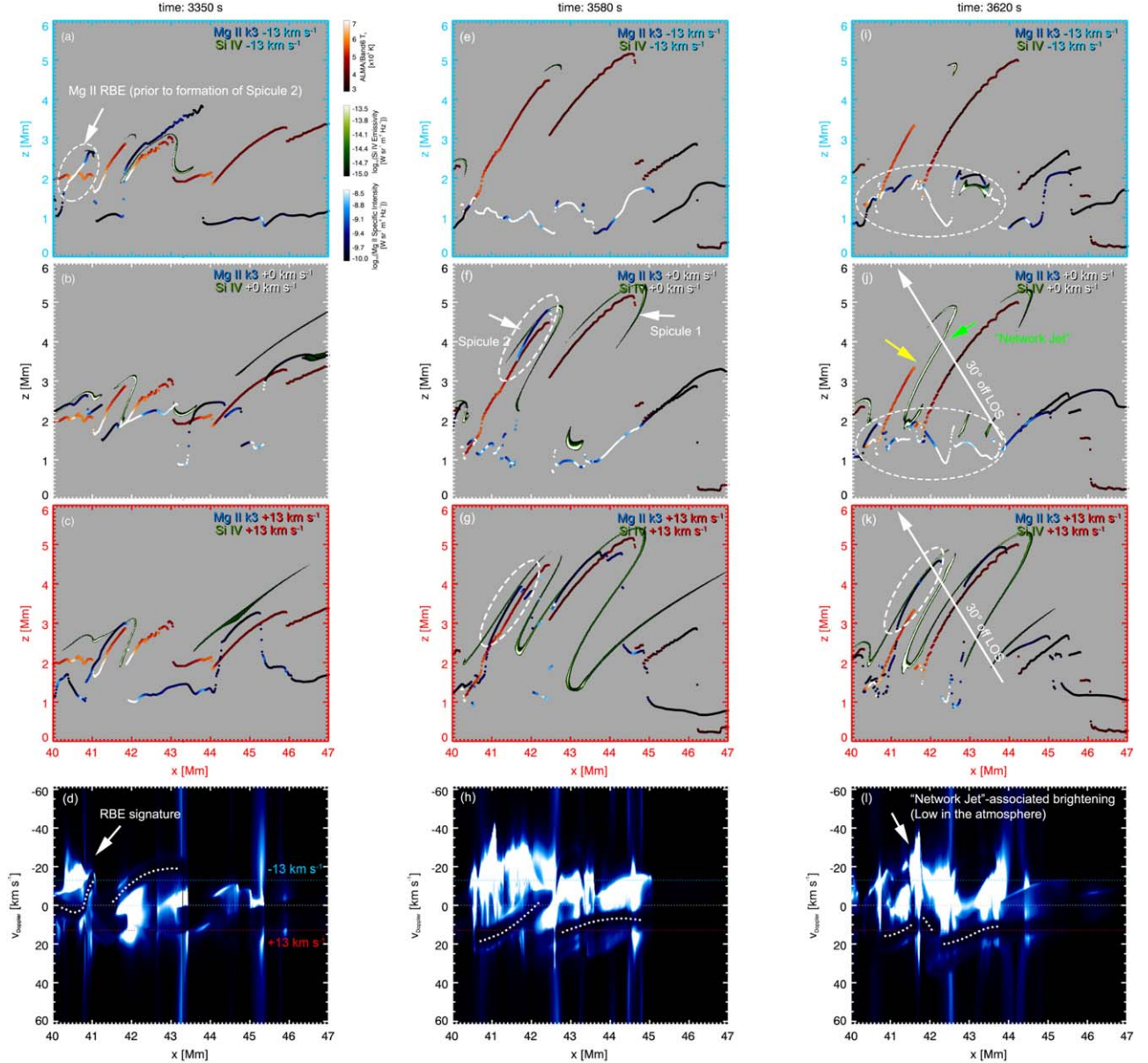


**Figure 6.** Maps from the simulation for the region with spicules, showing the spatial distribution of ALMA/Band6 emission from the spicules (at a height of  $\tau = 1$ ), along with Si IV emissivity and Mg II k specific intensity (at a height of  $\tau = 1$ ) at three different wavelength positions (corresponding to  $-13$ ,  $0$ , and  $+13$   $\text{km s}^{-1}$ ) and at three different times (one per column). Note that at all times (at least until the brightening of the spicule at 3620 s; yellow arrow) ALMA/Band6 follows closely the parts of the spicule emitting in Si IV. At 3620 s, brightening occurs when the spicular mass recedes back to the surface, showing significant emission at redshifts ( $+13$   $\text{km s}^{-1}$ ). The bottom row shows the Mg II  $\lambda$ - $x$  plot with colored dotted lines denoting the wavelength positions shown above. The dark band seen in the spectra is a well-developed k3 component in Mg II k (parts of it traced by a white dotted line). See text for discussion. An animated version of this figure can be found in the online journal. The animation proceeds from the simulation time of 3240–3750 s.

(An animation of this figure is available.)

effect develop as (i) bright Si IV, (ii) bright ALMA/Band6, and (iii) dark Mg II k, since the high intensity in Mg II k would be at the root of the spicule and the emission of (i) and (ii) would be projected against an area of low Mg II k background emission (e.g., for  $x > 44$  Mm). This example illustrates one of the possible reasons that at certain locations in the observations Mg II intensity is anticorrelated to both Si IV and ALMA/Band6.

The relationship of the ascending/descending phases of mass motions to Doppler shift and emissivity in Si IV is also seen in the plage region of the simulation (Figure 7). At  $t = 3400$  s a dynamic fibril shoots mass upward ( $x = [27, 29]$  Mm), where in the blue wing a “front” of Si IV emissivity is

closely followed by emission in ALMA/Band6 (panel (a); dashed oval). Mg II k intensity comes from greater geometric heights but in absorption, again in contrast to other locations in the domain, which are brighter but are at much lower geometric heights ( $z \approx 0.5$ – $1$  Mm). Similarly, relatively low intensity is seen at the nominal rest wavelength of Mg II k (panel (b)). This again pinpoints the reasons behind the anticorrelation we noted between Mg II k and the well-correlated pair of ALMA/Band6 and Si IV, both in the simulation and in the observations of plages. Moving forward to the times of the other two time steps ( $t = 3510$  s and  $3580$  s), we see a consistent evolutionary pattern between ALMA/Band6 and Si IV. That is, when the bulk of the mass in the dynamic fibril stalls, we get emission



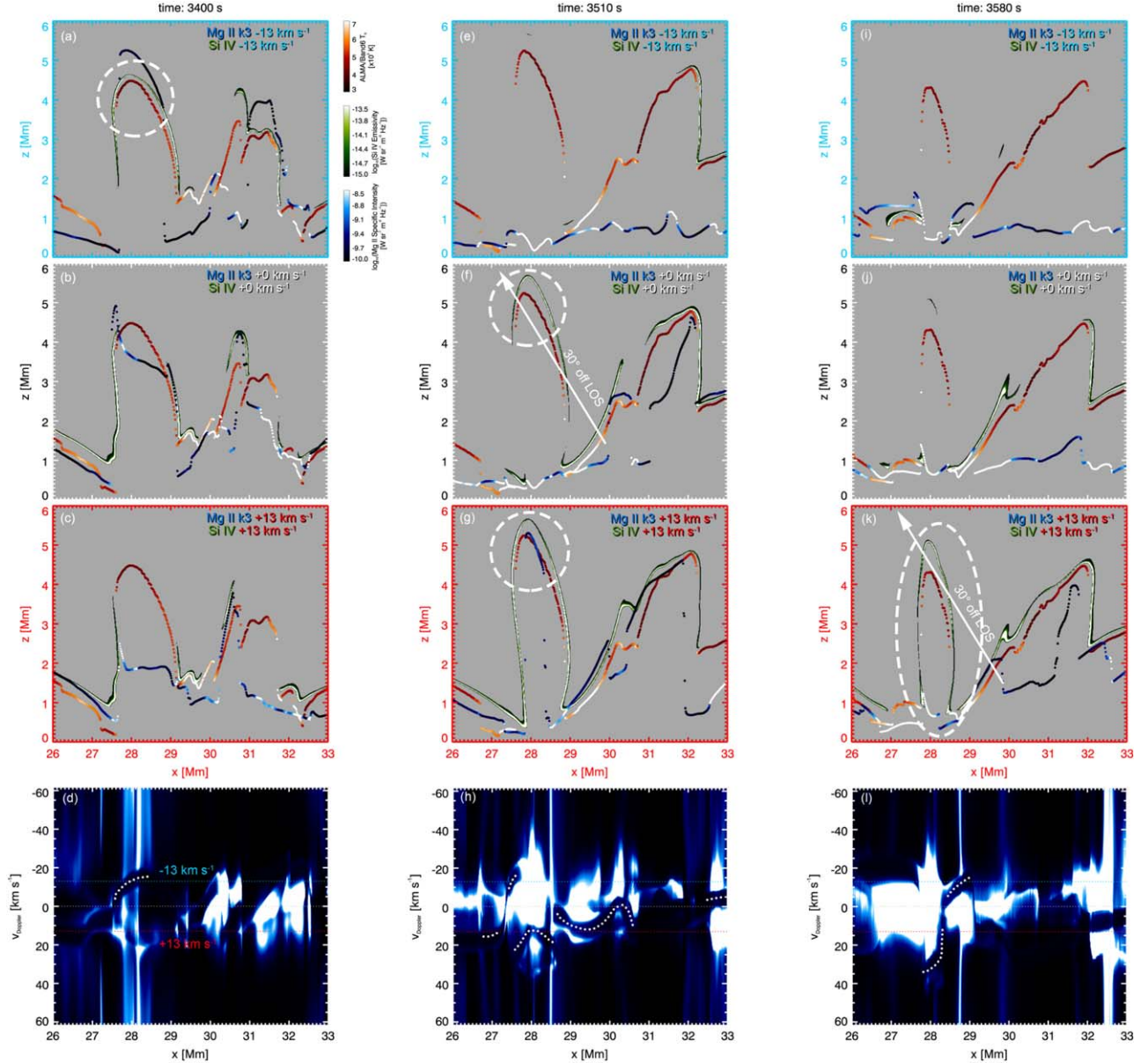


**Figure 7.** Maps from the simulation for the plage region, showing the spatial distribution of ALMA/Band6 emission and intensity/emissivity from IRIS observables at three different wavelength positions (corresponding to  $-13$ ,  $0$ , and  $+13$   $\text{km s}^{-1}$ ) and at three different times (one per column, as in Figure 6). Note that the location of ALMA/Band6 emission follows the locations of emissivity in Si IV more closely than it does those of Mg II k intensity, which is consistent with the high degree of correlation of ALMA/Band6 with Si IV seen in plage regions both in the simulation and in the observations. As in the previous figure, the bottom plots show the Mg II  $\lambda$ - $x$  plot with colored dotted lines denoting the wavelength positions shown above. The dark band seen in the spectra is a well-developed k3 component in Mg II k (traced in part by a white dotted line). See text for discussion.

from the Si IV line core (panel (f)), and when the mass recedes back to the surface, Si IV emits in the red wing, again closely followed by ALMA/Band6 emission (panel (k)). We also note that at those times high intensity in Mg II k comes primarily from lower heights in the atmosphere (see panels (i), (j) and dashed oval in panel (k)).

Therefore, we conclude that ALMA is sensitive to the cool to warm plasma existing at the highest parts of spicules and dynamic fibrils but just below their tips. These locations are subject to shocks or other cooling/heating mechanisms (such as ambipolar heating or cooling by adiabatic expansion), which may raise the plasma to high temperatures, eventually causing it to emit in Si IV ( $T \approx 80,000$  K) or even lower temperatures. Subsequently, the temperature drops to a level that ALMA/

Band6 is sensitive to (8000–10,000 K), in geometric heights not far from those of transition-region temperatures. This finding gives insights on the multithermal nature of spicules (Chintzoglou et al. 2018). All of the above results in the high similarity between Si IV and ALMA/Band6 seen in the observations. With regard to Mg II k, depending on the viewing angle and on how clearly such effects are seen against the background, comparisons with the other observables may show a loss of correlation, or if there is regularity in the appearance and positioning of such structures within the FOV, anticorrelation may also arise (i.e., bright features in one observable/passband “complementing” dark structures in another). This seems to be reasonable when spicules or dynamic fibrils are bright in Si IV and ALMA/Band6 but

manifest as low-intensity features in Mg II (due to enhanced absorption and/or low intensity in comparison to Mg II k intensities from other locations; for the case of dynamic fibrils this may be related to similar effects that were seen in spacetime plots of bright grains in the work of Skogsrud et al. 2016).

#### 4.2. Measuring the Temperature Increase in the Aftermath of Shocks above the Plage

Apart from the weak-magnetic flux plage periphery, the common IRIS and ALMA/Band6 FOV contains parts of a strong-magnetic flux plage region that is very dynamic. In this subsection we focus on the dynamics seen in the plage region, and we explore the potential of ALMA/Band6 observations for measuring the plasma temperature and its time evolution in regions dominated by the passage of chromospheric shocks.

Here, with IRIS observing in Mg II k and Si IV we can see chromospheric shocks as they propagate higher in the chromosphere/transition region. Focusing on the northern part of the common IRIS and ALMA/Band6 FOV, we see a lot of recurrent activity as brightenings above the plage and also some plane-of-the-sky motions of bright dynamic fibrils. Chromospheric plages exhibit features known as dynamic fibrils, driven by slow-mode magnetoacoustic shocks that pervade the plage region (Hansteen et al. 2006; De Pontieu et al. 2007a; Langangen et al. 2008). From our 34 minute long-time series we calculated the autocorrelation at each pixel in the Mg II FOV to determine locations of activity segmented by the characteristic lifetimes of the signal, such as intensity modulations caused by chromospheric shocks. da Silva Santos et al. (2020) have reported a periodicity for shocks in Mg II k of 3.5–4 minutes in plages. In areas above the plage at Mg II k2v we found autocorrelation times of  $\approx 150$ –200 s but also some even “slower” locations of  $\approx 300$  s. Using this autocorrelation map as a guide, we selected a  $1'' \times 1''$  subregion (corresponding to  $3 \times 6$  pixels for IRIS rasters and  $6 \times 6$  pixels for ALMA/Band6) that is well within the plage (position  $(x, y) = (4, 17)''$  in the raster FOV of Figure 1) in order to explore if ALMA can be used to study chromospheric shocks. Within the selected region, we produced  $\lambda$ - $t$  plots for Si II and Mg II k IRIS rasters and extracted  $T_b$  from ALMA/Band6. Furthermore, to improve the contrast in the  $\lambda$ - $t$  plots we filtered them with an unsharp-mask image processing operation with a 5 pixel radius. Also, to enhance weak features that were still not visible in the wings of the lines, we produced the time derivative of the direct  $\lambda$ - $t$  maps. We present the results in Figure 8.

As a shock passes through the chromosphere above the plage, a typical behavior is seen in the  $\lambda$ - $t$  plots of the chromospheric lines: a blueshifted excursion slowly drifts toward the red wing of the line, until a new blueshifted excursion appears again and so on, producing a “sawtooth” pattern in the  $\lambda$ - $t$  plot. This sawtooth pattern is seen in Mg II k  $\lambda$ - $t$  with sudden increases of the intensity in the far-blue wing that sweep through the dark k3 core and then reach the red wing typically with a new enhancement in the blue wing (Figure 8(b); see enhancements above the yellow line in the blue wing). Similarly, blueshifted enhancements appear in Si IV (Skogsrud et al. 2016) in tandem with the excursions in Mg II k (Figures 8(b), (d)). We overplot the ALMA/Band6  $T_b$  over the  $\lambda$ - $t$  plots for the same selected region above the plage. Despite the data gaps in the ALMA/Band6 observations, the behavior

of  $T_b$  jumps is strikingly similar to the wavelength-drift trends due to the passage of shocks in the chromosphere. In Figures 8(a), (c) we enhance the signatures of the onsets of shocks in the time-derivative plots and mark them with arrows. In fact, when looking at the blue wing, we see the similarity of the  $\lambda$ - $t$  time evolution with ALMA/Band6 is more obvious for Si IV than for Mg II k (see prominent blueshifts in Si IV  $\lambda$ - $t$  plot in areas indicated by arrows 2–5 in panel (d)), which may have to do with the similarity of ALMA/Band6 mm emission formation height to Si IV that we determine in the present paper. This result may also be consistent with da Silva Santos et al. (2020), who through inversions determined that during the passage of shocks ALMA/Band6 emission appears to emerge from lower optical depths.

Our interpretation is that ALMA/Band6 observations in plages are sensitive to the localized heating of the upper chromosphere/lower transition region produced by the passage of shocks. The jumps in  $T_b$  are of the order of 10%–20% from a baseline value of  $\approx 7500$  K (maximum jump at 8500 K). The observed decay time down to the baseline value is of the order of  $\approx 60$ –120 s. However, note that for Si IV  $\lambda$ - $t$  the signal in the selected pixel position in the raster occasionally becomes poor due to low photon counts in the FUV range of IRIS. The  $3 \times 6$  pixels for IRIS seems to improve the signal. We also note that the bright signatures of shocks seen in the rasters are not confined to one pixel location and appear to move in the plane of the sky until they fade. Again, the  $3 \times 6$  pixel window compensates for most of the plane-of-the-sky motions seen in the movie. There are times when the recurrence of brightenings takes place every  $\approx 120$  s (at least in the early phase of the plots; see arrows 1–3 in panel(b)). This may suggest that a given location above the plage may be pervaded by shocks coming from different directions at comparable timings. Such occasions may cause the periodicity patterns to modulate with shorter or even irregular periods. In addition, note that the spatial resolution of the ALMA/Band6 maps is significantly worse than that of the IRIS rasters (by approximately one order of magnitude); thus the filling factor of the shock (at the ALMA/Band6 beam size) is less than 1 (as compared to the spatial scales resolved with IRIS). Therefore, even though such 1000 K jumps in mm emission appear consistent with heating due to shocks as suggested by Wedemeyer-Böhm et al. (2007), we conclude that the true temperature enhancements may be even higher locally. Nevertheless, our work presents indications of localized heating of chromospheric plasma in plage regions by shocks that travel through the geometric height of formation of ALMA/Band6 free-free emission.

## 5. Discussion on Discrepancies with Previous Studies

Detailed comparison between  $T_{\text{rad}}$  (EUV) and  $T_b$  (mm wavelengths) in spatially resolved morphological features has recently become possible thanks to the high-resolution and high-cadence ALMA observations. High positive correlations for Mg II  $T_{\text{rad}}$  and ALMA/Band6  $T_b$  have been reported in the literature for regions of plages (e.g., Bastian et al. 2017, 2018; Jafarzadeh et al. 2019). However, the C.C. we found for Mg II and ALMA/Band6 (see Section 4.1.2) lies in the low end of those reported in previous studies. Below we explore the methodology used in previous studies in an attempt to replicate the higher C.C. reported for Mg II  $T_{\text{rad}}$  and ALMA/Band6  $T_b$  and to pinpoint the cause of the discrepancies with our results.



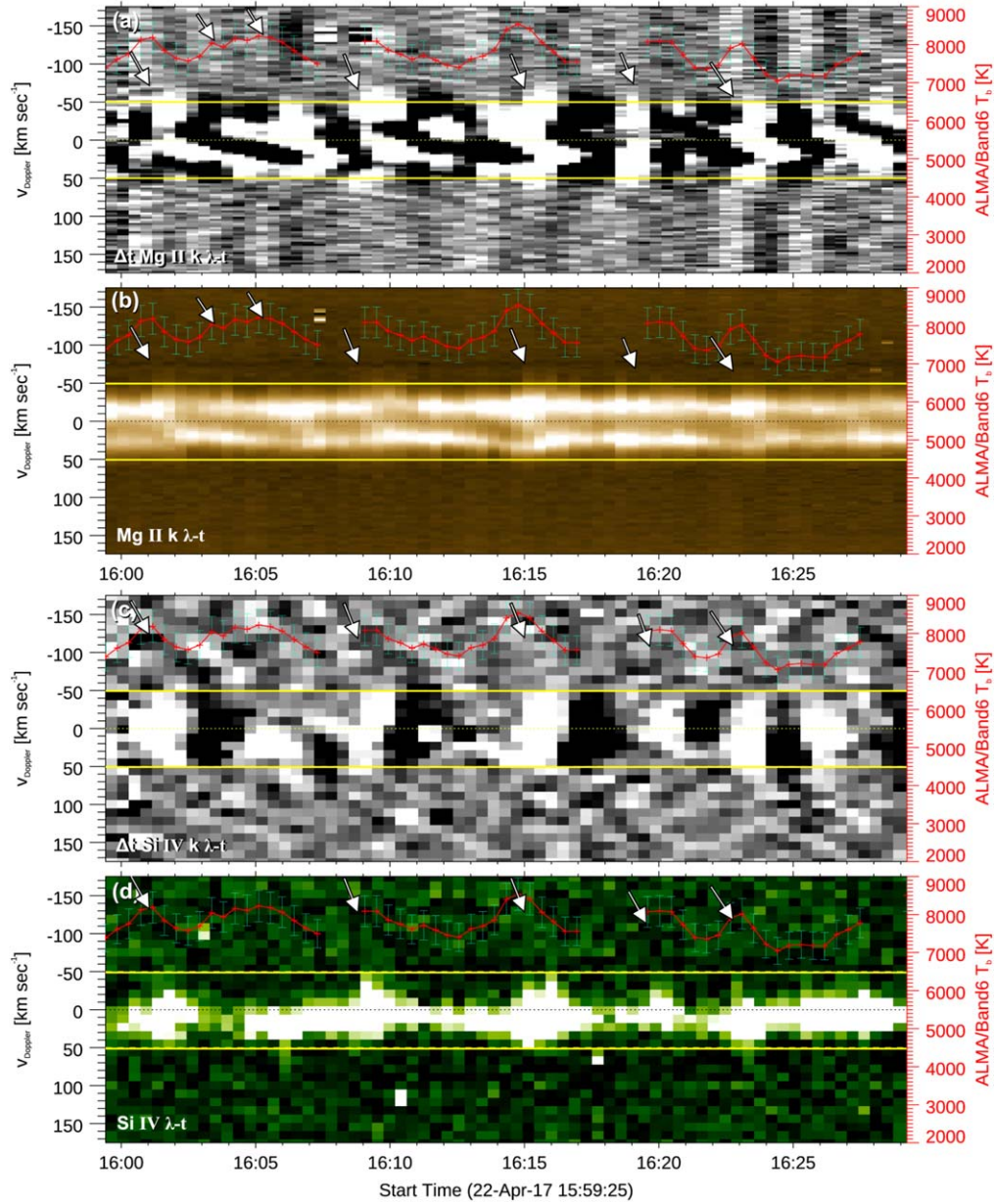


**Figure 8.** Top panels:  $\lambda$ - $t$  plots for Mg II k (b) and its time derivative (a) for the selected  $1'' \times 1''$  area above a plage region with recurrent shocks. Bottom panels: Si IV (d) and its corresponding time derivative (c). The  $\lambda$ - $t$  panels are unsharp-masked to improve contrast in the presentation of the figure. In all panels we overplot the ALMA/Band6  $T_b$ . The error bars correspond to 5% uncertainty in  $T_b$  values. The rest-wavelength position is plotted with a dotted line in all panels. Note the correlation of increases in  $T_b$  and blueshifts, suggesting chromospheric heating due to the passing of shocks in Si IV and Mg II (indicated by arrows).

Bastian et al. (2018) compared  $T_{\text{rad}}$  of Mg II h to ALMA/Band6  $T_b$  and reported a very high C.C. = 0.80 for plages. To perform a comparison we should first discuss the differences between our work and that of Bastian et al. (2018). First, the  $T_{\text{rad}}$  in Bastian et al. (2018) was produced from maps of the average  $T_{\text{rad}}$  of Mg II h2v and h2r including single-peak Mg II h profiles. Here, we integrate Mg II k over  $0.7 \text{ \AA}$ . The observing program that obtained the observations in Bastian et al. (2018) did not allow for a good synchronization between the IRIS and ALMA observables. In the present study, we obtained IRIS/ALMA observations with a less restrictive observing program to achieve minimal time differences among all observables. We also note that Bastian et al. (2018) determined plage regions with different criteria from ours (Section 3): they were based on the visual identification of prominent morphological features in

the FOV (i.e., contours roughly containing high Mg II h2v and h2r average  $T_{\text{rad}}$  and  $T_b$  for plages; Bastian et al. 2017, Figure 1(f) therein). Here we employ strict criteria for the definition of a plage and its periphery, based on the methodology presented in Section 3. However, given the large discrepancy in the C.C. (i.e., the C.C. reported in Bastian et al. (2018) is 40% larger than our value), here we also calculate  $T_{\text{rad}}$  in the same way as in Bastian et al. (2017, 2018). That is, we calculated  $T_{\text{rad}}$  for the average Mg II h2v and h2r line. After doing so, we found that the C.C. in that case was even lower, i.e., C.C. = 0.52, yielding an even larger discrepancy between our results and the results reported in Bastian et al. (2018; i.e., 54% larger than our value).

One possibility behind the discrepancy mentioned above is that the visual criteria employed for the definition of plages in Bastian et al. (2018) allowed the inclusion of low  $T_{\text{rad}}$  and  $T_b$

areas in plages. For instance, the lower plage mask in Figure 1(f) of Bastian et al. (2017) clearly shows lower intensities for the majority of the pixels therein. Thus, such pixels should not be classified as plages, given the consideration we make in this paper (see Section 3). The high C.C. of 0.80 that this study reported between Mg II h and ALMA/Band6  $T_b$  was obtained for the entire common FOV. We emphasize that such high correlation is not surprising if we consider the overall similarity over a diverse set of features present within that FOV, such as plages, sunspot umbras, and penumbras/superpenumbras, which as a whole appear morphologically similar between Mg II h  $T_{\text{rad}}$  and ALMA/Band6  $T_b$ . For example, if we take a region with a sunspot umbra, i.e., a morphological feature that is darker than the average intensity in the entire FOV in Mg II h, it also appears dark in ALMA/Band6 (compare Bastian et al. 2017, Figures 1(a), (c) therein). This equivalence also holds true for plage regions, which stand out as regions of higher intensity in either chromospheric observable. Thus, mixing regions with low  $T_{\text{rad}}$  and  $T_b$  (e.g., sunspot umbras, plage periphery, pores) together with brighter regions and treating this mix as a “plage” may effectively increase the C.C. A quick comparison between our correlation matrix for the full FOV (mixed) and that for the plage in Figure 3 supports our view. The mixed correlation matrix treats all plage and plage periphery points as one population (still excluding the pore). While the C.C. for ALMA/Band6  $T_b$  with Mg II k  $T_{\text{rad}}$  is 0.56 for the plage and 0.57 for the periphery, the calculation for the full FOV increases the value dramatically, to a C.C. of 0.74, which amounts to 90% of the value reported in Bastian et al. (2018). The total number of pixels in the plage mask is 650, which finally becomes 578 pixels after excluding the pore region (recall that we performed binning of 4 pixels along the y-direction). The total number of points in the periphery is 480. Thus, the inclusion of an additional 80% of plage periphery pixels (with about two-thirds showing low intensities) in the designated plage area made a clear difference in the C.C. between ALMA/Band6  $T_b$  and Mg II k. While we cannot exclude the possibility of additional factors behind this discrepancy (e.g., variability between different solar regions, the different calibration methods employed in Bastian et al. (2018), and the fact that the pixels in IRIS and ALMA observations were not selected based on minimal time difference constraints), including quieter pixels within plage regions may play a significant role in increasing the C.C. from a marginal value (0.56) to a value suggesting high positive correlation (0.80).

A study by Jafarzadeh et al. (2019) focused on ALMA/Band6 and IRIS observations of the same region analyzed in Bastian et al. (2018). This work also investigated relationships between  $T_b$  from ALMA/Band6 and  $T_{\text{rad}}$  from IRIS Mg II k and h (for each line component), C II, and intensities of the optically thin Si IV and O I. Their region of plage was defined with a quantitative method, i.e., as a chromospheric region above photospheric magnetic fields of  $\geq \pm 0.2$  kG, a threshold value not too different from the one we use here. Indeed our magnetic map will not change if we use either  $\pm 0.1$  kG or  $\pm 0.2$  kG for thresholds. However, we point out that their methodology leads to the inclusion of areas in the sunspot penumbra/superpenumbra that in Bastian et al. (2018) were excluded from the plage areas. Nevertheless, the region designated as a plage in Jafarzadeh et al. (2019) above the superpenumbra/penumbra comprised the vast majority of the

plage pixels in that work. To this we add that the regions of plages used in Bastian et al. (2018) are only partially included within the FOV in Jafarzadeh et al. (2019; i.e., the similarity of plage regions selected for the statistical studies in these two works is further reduced). All these factors render comparison with Bastian et al. (2018) a difficult task. To keep this discussion focused we moved some details to the Appendix.

In contrast to Bastian et al. (2018), who calculated the C.C. between ALMA/Band6  $T_b$  and the mean  $T_{\text{rad}}$  from Mg II h2v and h2r, the C.C. values in Jafarzadeh et al. (2019) were calculated separately for each individual line feature of Mg II  $T_{\text{rad}}$  with ALMA/Band6  $T_b$ ; namely, for ALMA/Band6  $T_b$  versus  $T_{\text{rad}}$  from Mg II k2v (k2r) the C.C. was 0.73 (0.80) and 0.68 (0.78) for Mg II h2v (h2r). Comparatively, ALMA/Band6 with Mg II k2v (k2r) was 48% (49%) higher than those calculated from our data set of plages with line fitting; as for Mg II h2v (h2r), that was 39% (42%) higher than our values. Reconciling all the differences we have mentioned between the work of Jafarzadeh et al. (2019) and our study and also considering the fact that both studies focused on pixels with the least time difference possible, we understand the discrepancies between our scatter plots and theirs to be due to their inclusion of pores or superpenumbra pixels in their statistics. If we do the same experiment we did earlier in our comparison to Bastian et al. (2018) and we include the periphery in our calculations, then the C.C. reported in Jafarzadeh et al. (2019) for Mg II k2v (k2r) will be only 7% (14%) higher than those calculated from our data set, and for Mg II h2v (h2r), that will be only 2% (11%) higher than ours. In Figures 3 and 5(e) of Jafarzadeh et al. (2019) the ALMA and IRIS maps and the map showing the mask used for plages are provided. By consulting the time difference map between the ALMA and IRIS pixels shown in Figure 4(f) therein, we can identify exactly which parts of the plage were used in the scatter plots of Figure 13 therein. There appear to be several locations with radial dark “lanes” or “streaks” of low  $T_{\text{rad}}$  and  $T_b$  around the superpenumbra/penumbra, and the majority of these pixels were used in the plage scatter plots of Jafarzadeh et al. (2019). Therefore, it is possible that the similarity of the results for plages reported by Jafarzadeh et al. (2019) and Bastian et al. (2018) and their discrepancy with our results may have the same origin: the differences in the criteria used in distinguishing regions of plages from neighboring regions on the Sun.

## 6. Summary and Conclusions

In this work we focus on addressing the nature and the dynamics of chromospheric/transition-region structures found in plages, namely, fibrils, jetlike features (Type II spicules are covered in a companion paper, Chintzoglou et al. 2021), and traveling shocks, using high-cadence and high-spatial resolution data from the ALMA and IRIS observatories. We employed a 2.5D numerical simulation (Bifrost model) of a plage region considering ambipolar diffusion in nonequilibrium ionization conditions. We produced synthetic observables to compare the model with our observations from ALMA/Band6 and IRIS. Lastly, we performed a first-cut study of the heating of the chromosphere above plages by measuring brightness temperature modulation due to passing shocks with ALMA/Band6.

Below we summarize our findings:



1. We report a very high degree of similarity for features seen in plages between ALMA/Band6 and IRIS/SJI 1400 Å and Si IV 1393 Å rasters (Figure 1). We conclude that ALMA/Band6 is sensitive to the cool plasma at the highest parts of spicules and dynamic fibrils (i.e., in plages), which follows (because of the locally large temperature gradients) plasma that emits in Si IV ( $T \approx 80,000$  K, transition-region temperatures; this result also provides support to the work of Rutten 2017).
2. We present observations showing anticorrelation between intensity features seen in Si IV and Mg II IRIS rasters (with intensity depressions of Mg II k highlighted in Figure 1). We conclude that the apparent anticorrelation or lack of correlation has its origin in Mg II opacity effects in plage structures. Strong absorption is the reason behind the low Mg II intensities emerging from greater geometric heights in the locations of spicules (Figure 6).
3. For plages we report a low linear C.C. ( $0.49 \leq C.C. \leq 0.55$ ) for ALMA/Band6  $T_b$  with Mg II for any of the k2v/k2r/h2v/h2r line features and a maximum of 0.56 for wavelength-integrated Mg II k that contains the k2v, k3, and k2r line features. Our results are quantitatively in contrast with those of previous works (e.g., Bastian et al. 2018; Jafarzadeh et al. 2019). We also determined that including quieter areas in the plage sample, i.e., considering a mixed area of plage and plage periphery as a “plage,” greatly increased the C.C. between ALMA/Band6  $T_b$  and  $T_{\text{rad}}$  from Mg II k and h, producing values as high as those in Bastian et al. (2018) and Jafarzadeh et al. (2019). We thus caution on the different criteria employed for defining plage regions, which may skew quantitative studies of correlations between different observables.
4. The spatial extent of a plage is not formally well defined in previous literature. Here, our empirical approach focuses on isolating a plage from its surroundings in a different manner from previous approaches (Section 3). We also add that the C.C. is a very sensitive statistical measure. A small amount of outliers in a scatter plot can greatly affect the C.C. value. Thus given the high sensitivity of the C.C. and its application in cases where plages cannot be robustly classified with conventional techniques (e.g., due to the presence of pores or to being too close to sunspot penumbras), we caution that the C.C. values between  $T_{\text{rad}}$  and  $T_b$  in plages can actually be lower, i.e., as low as we report in the present paper.
5. It has been previously reported (Bastian et al. 2017; Jafarzadeh et al. 2019) that there is scatter between radiative temperatures from Mg II and brightness temperatures from ALMA/Band6, with a suggested cause of the scatter being the decoupling of the Mg II source function from the local conditions. Our work demonstrates that the scatter is more significant than previously thought, and highlights another reason behind its nature: both the observations and the simulation suggest that the formation height for ALMA/Band6 emission is above that of Mg II for most wavelengths along the Mg II line, even though both Mg II and ALMA/Band6 are sensitive to a similar range of temperatures. This formation height difference can contribute to the large scatter. We caution that the model should not be taken as a perfect representation of the plage atmosphere. For example,

the distribution of modeled brightness temperatures of ALMA/Band6 is lower by 2000 K as compared to the observations.

6. We performed a thorough quantitative study of the similarities between time-averaged Si IV, C II (wavelength-integrated intensities), Mg II k (average  $T_{\text{rad}}$ ), and ALMA/Band6 ( $T_b$ ) maps (Figure 3). We report that the highest C.C. was obtained between any combination of the triad of Si IV, C II, and ALMA/Band6, and the lowest C.C. was obtained between Mg II k–Si IV and Mg II k–ALMA/Band6. Additionally, C II was found to have moderate to high C.C. with all other observables. We conclude that this study provides evidence on the general tendency for the order of the formation heights of all these different observables with geometric height. That is, the Mg II k (wavelength-integrated) intensity ( $T_{\text{rad}}$ ) emerges from lower geometric heights in the plage atmosphere, with Si IV forming at the greatest heights (with a formation temperature  $T \approx 80,000$  K, placing it in the transition region). The good agreement of C II with all other observables is due to its having, on average, a formation height between those of Mg II k and Si IV. This result seems consistent with the work of Rathore et al. (2015b) based on analysis of a numerical simulation.
7. We present indications of heating by shocks propagating in the chromosphere with ALMA/Band6 (beam size  $\approx 0''.7 \times 0''.8$ ). We found a repetitive increase-and-decrease of the local chromospheric plasma temperature above plages of the order of 10%–20% from a basal value of 7500 K (for comparison, the temperature for a location in the periphery of a plage was found to be  $\approx 5500$  K), with a decay time back to the baseline of about 60–120 s (Figure 8). We found indications of a recurrence at around 120 s. This may suggest that a specific location in a plage may be pervaded by shocks coming from different directions and at different timings, leading to intensity (and  $T_b$ ) modulations of shorter (or even irregular) periods. da Silva Santos et al. (2020) performed inversions of IRIS with ALMA and reported that emission from shocks in the ALMA/Band6 plage may come from lower optical depths (i.e., greater geometric heights) as compared to weakly magnetized areas (e.g., plage periphery). This is consistent with our determination of the formation height for ALMA/Band6, which seems to be just below that of Si IV.

This work demonstrates the benefits of the synergy between ALMA and IRIS observations, which effectively expands the diagnostic capabilities of each observatory, and also tested and provides constraints for advanced numerical simulations.

This paper makes use of the following ALMA data: ADS/JAO.ALMA#2016.1.00050.S. ALMA is a partnership between the European Southern Observatory (ESO; representing its member states), the National Science Foundation (NSF; USA), and NINS (Japan), together with NRC (Canada), MOST and ASIAA (Taiwan), and KASI (Republic of Korea) and in cooperation with the Republic of Chile. The Joint ALMA Observatory is operated by ESO, AUI/NRAO, and NAOJ. We gratefully acknowledge support by NASA contract NNG09FA40C (IRIS). J.M.S. is also supported by NASA grants NNX17AD33G and 80NSSC18K1285 and NSF grant AST1714955. V.H. is supported by NASA grant

80NSSC20K1272. J.C.d.I.R. is supported by grants from the Swedish Research Council (2015-03994), the Swedish National Space Board (128/15), and the Swedish Civil Contingencies Agency (MSB). This project has received funding from the European Research Council (ERC) under the European Union’s Horizon 2020 research and innovation program (SUNMAG, grant agreement 759548). M.S., S.J., and S.W. are supported by the SolarALMA project, which has received funding from the ERC under the European Union’s Horizon 2020 research and innovation program (grant agreement No. 682462), and by the Research Council of Norway through its Centres of Excellence scheme, project number 262622. The simulations and Mg II synthesis were run on clusters from the Notur project and the Pleiades cluster through computing projects s1061, s1630, and s2053 from the High-end Computing division of NASA. This research is also supported by the Research Council of Norway through its Centres of Excellence scheme, project number 262622, and through grants of computing time from the Programme for Supercomputing. IRIS is a NASA small-explorer mission developed and operated by LMSAL with mission operations executed at the NASA Ames Research Center and major contributions to downlink communications funded by the European Space Agency and the Norwegian Space Centre. HMI and AIA are instruments on board SDO, a mission for NASA’s Living with a Star program.

## Appendix










To improve the readability of the main text we host here part of the discussion found in Section 5, where we highlight the large discrepancies between our results (and our methodology) and those of previous studies (e.g., Bastian et al. 2018; Jafarzadeh et al. 2019). In particular, here we highlight the effects due to the inclusion (or insufficient exclusion) of pores in plages as a source of bias, and we also emphasize our unprecedented time synchronization between rapid EUV rasters and rapid mm emission imaging observations in comparison to that achieved by previous studies.

In contrast to Bastian et al. (2018), Jafarzadeh et al. (2019) attempted to remove pores within the plage by applying a mask derived from an HMI photospheric magnetogram with magnetic field values of  $\geq \pm 0.8$  kG. However, we note here that the small size of the pores in that plage cannot be fully accounted for by the simple application of a mask from a photospheric magnetogram, due to the natural expansion of fields as they reach chromospheric and transition-region heights. Conversely, this causes any pore region mask produced from observations at the photosphere to contain only a part of the associated area higher up, making the safe extraction of pores from the immediate plage a challenging task. This is due to superposition effects and confusion along the LOS of structures in the chromospheric data. The definition of pore regions within plages in Jafarzadeh et al. (2019) appears to include real plage signals. In Figures 6 and 7 of Jafarzadeh et al. (2019) we can see that the pore signal is included in the histograms done for other regions in the FOV, namely, “penumbra and pores” and “sunspot and pores,” where Mg II k2v, k2r, h2v, and h2r are clearly skewed to higher  $T_{\text{rad}}$  with a sharp drop at 6000 K. However, the histograms for “umbra” and “quiet regions” are clearly skewed to the low end of  $T_{\text{rad}}$  with a very gradual drop toward 6000 K. Thus, they share similarities to the histograms for “plage,” justifying our

concerns for proper characterization of plages from non-plage regions. In our work here, while we did not study the region above the pore, we safely excluded it by applying a threshold on ALMA/Band6  $T_b$ ; this allowed us to account for more extended boundaries of structures as they expanded from the photosphere to the chromosphere, leaving behind a clean map for plages (Figure 3).

Also, we note that Jafarzadeh et al. (2019) divided the ALMA/Band6 data into four sub-bands and only used the one at  $\lambda = 1.3$  mm, instead of taking the average of all sub-bands as in Bastian et al. (2018) and our present work. Such averaging results in Band6 maps at  $\lambda = 1.25$  mm. Finally, Jafarzadeh et al. (2019) strived to take into account time differences between the ALMA/Band6 mosaic and the scanning time of the large IRIS raster. Unfortunately, due to the nature of the mosaicking scanning process of these particular ALMA/Band6 observations (complicated since it does not follow the scanning direction of the IRIS raster, which takes a nontrivial amount of time) the authors had only a limited number of pixels with a minimal time difference in their data set. Thus, despite attempts to match the time between pixels from ALMA and IRIS, an adequate number of pixels for their statistics was obtained only after allowing for a variable matching of the sampling time, i.e., one spanning 0.5–2 minutes (Figure 4(f) in Jafarzadeh et al. 2019). In addition, the same work explored correlations between observables by limiting time differences to 0.5 minutes at the expense of sample number. In comparison, Bastian et al. (2018) did not select pixels with such criteria; thus significant chromospheric evolution was not captured in their analysis. As we mention in the beginning of Section 5, our sampling time synchronization between data sets is superb, i.e.,  $\pm 1$  s at worst, and is consistent throughout the data series analyzed in our work. This is due to the fast IRIS raster scanning times (26 s) for this particular observation and also thanks to the rapid cadence (2 s) of our ALMA/Band6 observations.

## ORCID iDs

Georgios Chintzoglou  <https://orcid.org/0000-0002-1253-8882>  
 Bart De Pontieu  <https://orcid.org/0000-0002-8370-952X>  
 Juan Martínez-Sykora  <https://orcid.org/0000-0002-0333-5717>  
 Viggo Hansteen  <https://orcid.org/0000-0003-0975-6659>  
 Jaime de la Cruz Rodríguez  <https://orcid.org/0000-0002-4640-5658>  
 Shahin Jafarzadeh  <https://orcid.org/0000-0002-7711-5397>  
 Sven Wedemeyer  <https://orcid.org/0000-0002-5006-7540>  
 Timothy S. Bastian  <https://orcid.org/0000-0002-0713-0604>  
 Alberto Sainz Dalda  <https://orcid.org/0000-0002-3234-3070>

## References

- Bastian, T. S., Chintzoglou, G., De Pontieu, B., et al. 2017, *ApJL*, **845**, L19
- Bastian, T. S., Chintzoglou, G., De Pontieu, B., et al. 2018, *ApJL*, **860**, L16
- Carlsson, M., De Pontieu, B., & Hansteen, V. H. 2019, *ARA&A*, **57**, 189
- Carlsson, M., Leenaarts, J., & De Pontieu, B. 2015, *ApJL*, **809**, L30
- Carlsson, M., & Stein, R. F. 1997, *ApJ*, **481**, 500
- Carlsson, M., & Stein, R. F. 2002, *ApJ*, **572**, 626
- Chintzoglou, G., De Pontieu, B., Martínez-Sykora, J., et al. 2018, *ApJ*, **857**, 73
- Chintzoglou, G., De Pontieu, B., Martínez-Sykora, J., et al. 2021, *ApJ*, **906**, 82, (Paper I)
- Chintzoglou, G., Vourlidas, A., Savcheva, A., et al. 2017, *ApJ*, **843**, 93



- Chintzoglou, G., Zhang, J., Cheung, M. C. M., & Kazachenko, M. 2019, [ApJ](#), **871**, 67
- da Silva Santos, J. M., de la Cruz Rodríguez, J., Leenaarts, J., et al. 2020, [A&A](#), **634**, A56
- De Pontieu, B., Hansteen, V. H., Rouppe van der Voort, L., van Noort, M., & Carlsson, M. 2007a, [ApJ](#), **655**, 624
- De Pontieu, B., McIntosh, S. W., Carlsson, M., et al. 2007b, [Sci](#), **318**, 1574
- De Pontieu, B., Title, A. M., Lemen, J. R., et al. 2014, [SoPh](#), **289**, 2733
- Deslandres, H. 1893, KIMS, **16**, 230
- Hansteen, V. H., De Pontieu, B., Rouppe van der Voort, L., van Noort, M., & Carlsson, M. 2006, [ApJL](#), **647**, L73
- Harvey, K., & Harvey, J. 1973, [SoPh](#), **28**, 61
- Jafarzadeh, S., Wedemeyer, S., Szydlarski, M., et al. 2019, [A&A](#), **622**, A150
- Langangen, Ø., De Pontieu, B., Carlsson, M., et al. 2008, [ApJL](#), **679**, L167
- Loukitcheva, M., Solanki, S. K., Carlsson, M., & White, S. M. 2015, [A&A](#), **575**, A15
- Martínez-Sykora, J., De Pontieu, B., de la Cruz Rodríguez, J., & Chintzoglou, G. 2020a, [ApJL](#), **891**, L8
- Martínez-Sykora, J., Leenaarts, J., De Pontieu, B., et al. 2020b, [ApJ](#), **889**, 95
- Pesnell, W. D., Thompson, B. J., & Chamberlin, P. C. 2012, [SoPh](#), **275**, 3
- Rathore, B., Carlsson, M., Leenaarts, J., & De Pontieu, B. 2015a, [ApJ](#), **811**, 81
- Rathore, B., Pereira, T. M. D., Carlsson, M., & De Pontieu, B. 2015b, [ApJ](#), **814**, 70
- Rutten, R. J. 2017, [A&A](#), **598**, A89
- Schmit, D., Bryans, P., De Pontieu, B., et al. 2015, [ApJ](#), **811**, 127
- Secchi, A. 1877, Le Soleil. Seconde Partie. Structure du Soleil (suite)—Activité extérieure (Paris: Gauthier-Villars)
- Skogsrud, H., Rouppe van der Voort, L., & De Pontieu, B. 2016, [ApJ](#), **817**, 124
- Wedemeyer, S., Szydlarski, M., Jafarzadeh, S., et al. 2020, [A&A](#), **635**, A71
- Wedemeyer-Böhm, S., Ludwig, H. G., Steffen, M., Leenaarts, J., & Freytag, B. 2007, [A&A](#), **471**, 977
- Wootten, A., & Thompson, A. R. 2009, [IEEEP](#), **97**, 1463
- Yurchyshyn, V. B., Wang, H., & Goode, P. R. 2001, [ApJ](#), **550**, 470
- Zhang, J., Solanki, S. K., & Wang, J. 2003, [A&A](#), **399**, 755